

KRONECKER FACTORIZATION IMPROVES EFFICIENCY AND INTERPRETABILITY OF SPARSE AUTOENCODERS

000
001
002
003
004
005 **Anonymous authors**
006 Paper under double-blind review
007
008
009
010

ABSTRACT

011 Sparse Autoencoders (SAEs) have demonstrated significant promise in interpreting
012 the hidden states of language models by decomposing them into interpretable latent
013 directions. However, training and interpreting SAEs at scale remains challenging,
014 especially when large dictionary sizes are used. While decoders can leverage
015 sparse-aware kernels for efficiency, encoders still require computationally intensive
016 linear operations with large output dimensions. To address this, we propose Kron-
017 SAE – a novel architecture that factorizes the latent representation via Kronecker
018 product decomposition, drastically reducing memory and computational overhead.
019 Furthermore, we introduce mAND, a differentiable activation function approximating
020 the binary AND operation, which improves interpretability and performance in
021 our factorized framework.
022

1 INTRODUCTION

023 Interpreting large language models and their embeddings in particular remains a central challenge
024 for transparency and controllability in AI systems (Elhage et al., 2023; Heap et al., 2025). Sparse
025 autoencoders (SAEs) have emerged as powerful tools for uncovering human-interpretable features
026 within neural activations by enforcing activation sparsity to induce discrete-style dictionaries (Elhage
027 et al., 2023; Gao et al., 2025; Cunningham et al., 2024). These dictionaries facilitate circuit-level
028 semantic analysis (Marks et al., 2025) and concept discovery, enabling fine-grained probing of model
029 internals (Elhage et al., 2023; Cunningham et al., 2024).
030

031 However, naively scaling SAEs to the widths demanded by modern transformers leads to prohibitive
032 compute costs, limiting their applicability to large-scale interpretation experiments. *Gated* SAEs
033 (Rajamanoharan et al., 2024a) address this by learning continuous sparsity masks via lightweight
034 gating networks, and *Switch* SAEs (Mudide et al., 2025) leverage conditional computation by routing
035 activations among smaller expert SAEs, reducing computation by activating only a subset of experts
036 per input. Gao et al. (2025) propose an acceleration of TopK SAE that utilizes an optimized kernel
037 based on efficient sparse–dense matrix multiplication. Encoder remains unoptimized: it still performs
038 a dense projection into the full dictionary, incurring high computational cost and limiting scalability.
039

040 Another limitation of SAEs is the absence of structure within learned latents in its classical design.
041 While Mudide et al. (2025) address this via expert subnetworks, Bussmann et al. (2025) imposes
042 feature hierarchy via nested dictionaries structure and improves the interpretability of SAE latents.
043

044 In this paper we address both these directions and introduce **KronSAE**, an encoder that is applicable to
045 many existing SAE architectures. By decomposing the latent space into head-wise Kronecker factors
046 and including differentiable logical AND-like gating mechanism, KronSAE reduces both parameters
047 and compute overhead while preserving reconstruction fidelity and improves interpretability.

048 This work makes three primary contributions:

- 049 1. We identify the encoder projection as one of the principal scalability bottlenecks in sparse
050 autoencoders, demonstrating that targeted encoder optimizations can significantly improve
051 computational performance while maintaining reconstruction quality.
- 052 2. We propose **KronSAE**, a Kronecker-factorised sparse autoencoder equipped with the novel
053 mAND activation function. The design reduces encoder cost and is compatible with existing
sparse decoder kernels, loss function designs and mixture of experts architecture.

054 3. We show on multiple language models that KronSAE decreases feature absorption and
 055 yields more interpretable latents under fixed compute.
 056

057 **2 RELATED WORK**
 058

059 **Sparse Autoencoders.** Early work demonstrated that SAEs can uncover human-interpretable
 060 directions in deep models (Cunningham et al., 2024; Templeton et al., 2024), but extending them
 061 to the large latent sizes ($F \gg d$) for modern language models with large hidden dimension d
 062 is expensive: each forward pass still requires a dense $\mathcal{O}(Fd)$ encoder projection. Most prior
 063 optimization efforts focus on the decoder side: for example, Gao et al. (2025) introduce a fused
 064 sparse–dense TOPK kernel that reduces wall-clock time and memory traffic, while Rajamanoharan
 065 et al. (2024a) decouple activation selection from magnitude prediction to improve the ℓ_0 –MSE
 066 trade-off. Separately, Rajamanoharan et al. (2024b) propose JUMPRELU, a nonlinearity designed to
 067 mitigate shrinkage of large activations in sparse decoders.
 068

069 **Conditional Computation.** These schemes avoid instantiating a full dictionary per token by
 070 routing inputs to a subset of expert SAEs via a lightweight gating network (Mudide et al., 2025)
 071 by employing the Mixture-of-Experts ideas (Shazeer et al., 2017), but still incur a dense per-expert
 072 encoder projection, leaving the encoder as the primary bottleneck.
 073

074 **Factorizations and Logical Activation Functions.** Tensor product representations (Smolensky,
 075 1990) have been utilized to represent the compositional structures in dense embeddings, closely
 076 resembling our idea of AND-like compositions, and recent studies have been extended TPR to
 077 study the transformer hidden states and in-context learning (Soulou et al., 2020; Smolensky et al.,
 078 2024). Separately, tensor-factorization methods have been used to compress large weight matrices in
 079 language models (Edalati et al., 2021; Wang et al., 2023), and structured matrices have been utilized
 080 to improve training efficiency and might be used to impose the inductive bias (Dao et al., 2022).
 081 In parallel, differentiable logic activations were introduced to approximate Boolean operators in
 082 a smooth manner (Lowe et al., 2021). Our method synthesizes these lines of work: we embed a
 083 differentiable AND-like gate into a Kronecker-factorized efficient encoder to build compositional
 084 features while preserving end-to-end differentiability.
 085

086 **3 METHOD**
 087

088 **Preliminaries.** Let $\mathbf{x} \in \mathbb{R}^d$ denote an activation vector drawn from a pretrained transformer. A
 089 conventional TopK SAE (Gao et al., 2025) produces a reconstruction $\hat{\mathbf{x}}$ of \mathbf{x} via
 090

$$\mathbf{f} = \text{TopK}(W_{\text{enc}}\mathbf{x} + \mathbf{b}_{\text{enc}}), \quad \hat{\mathbf{x}} = W_{\text{dec}}\mathbf{f} + \mathbf{b}_{\text{dec}}, \quad (1)$$

091 where $W_{\text{enc}} \in \mathbb{R}^{F \times d}$ and $W_{\text{dec}} \in \mathbb{R}^{d \times F}$ are dense matrices and $\mathbf{f} \in \mathbb{R}^F$ is a sparse vector retaining
 092 only the K largest activations. The encoder cost therefore scales as $\mathcal{O}(Fd)$ per token.
 093

094 **KronSAE.** Our method reduces the encoder’s computational cost while also enforcing compositional
 095 structure of the latents. We decompose the latent space into h independent heads, and each
 096 head k is parameterised by the composition of two thin matrices $P^k \in \mathbb{R}^{m \times d}$ (composition base) and
 097 $Q^k \in \mathbb{R}^{n \times d}$ (composition extension), with dimensions $m \leq n \ll d$ and $F = h m n$. The pre-latents
 098

$$\mathbf{p}^k = \text{ReLU}(\mathbf{u}^k) \quad \text{and} \quad \mathbf{q}^k = \text{ReLU}(\mathbf{v}^k), \quad (2)$$

099 with $\mathbf{u}^k = P^k \mathbf{x}$ and $\mathbf{v}^k = Q^k \mathbf{x}$ acting as the elements from which compositional features would be
 100 built, are combined through an element-wise interaction kernel independently in each head:
 101

$$z_{i,j}^k := \text{mAND}(u_i^k, v_j^k) := \begin{cases} \sqrt{u_i^k v_j^k}, & u_i^k > 0 \text{ and } v_j^k > 0, \\ 0, & \text{otherwise,} \end{cases} \quad (3)$$

102 where $\mathbf{z}^k \in \mathbb{R}^{m \times n}$; it is then flattened in a row-major order to a vector equivalent to the element-wise
 103 square root of the Kronecker product of \mathbf{p}^k and \mathbf{q}^k . Assuming that $\text{vec}(\cdot)$ is in row-order, we get
 104

$$\text{vec}(\mathbf{z}^k) = \sqrt{\text{vec}(\mathbf{p}^k(\mathbf{q}^k)^\top)} = \sqrt{\mathbf{p}^k \otimes \mathbf{q}^k} \quad (4)$$

Concatenating heads and applying TopK yields *post-latents* $\mathbf{f} \in \mathbb{R}^F$. By ensuring active $z_{i,j}$ only when $p_i > 0$ and $q_j > 0$ we directly force the AND-like interaction: let \mathcal{P} and \mathcal{Q} be the sets of hidden state vectors on which p_i and q_j , respectively, are active, and let \mathcal{F} be the set of inputs on which $z_{i,j} > 0$, then it is true that $\mathcal{P} \cap \mathcal{Q} = \mathcal{F}$. The square root in equation 3 prevents activation value explosion when both pre-latents are active. See additional discussion in Appendix C.

The encoder cost per token drops from $\mathcal{O}(Fd)$ to $\mathcal{O}(h(m+n)d)$ (see Appendix A.2). KronSAE thus reduces FLOPs and parameter count without routing overhead, and is orthogonal to existing sparse decoder kernels (Gao et al., 2025) and thus can be combined with them for end-to-end speed-ups.

4 EXPERIMENTS

We train SAEs on the residual streams of Qwen-2.5-1.5B-Base (Yang et al., 2024), Pythia-1.4B-deduped (Biderman et al., 2023), and Gemma-2-2B (Team et al., 2024) language models. Activations are collected on FineWeb-Edu, a filtered subset of educational web pages from the FineWeb corpus (Penedo et al., 2024). We measure reconstruction quality via explained variance (EV),

$$EV = 1 - \frac{\text{Var}(\mathbf{x} - \hat{\mathbf{x}})}{\text{Var}(\mathbf{x})},$$

so that 1.0 is optimal, and use automated interpretability pipeline (Bills et al., 2023; Paulo et al., 2024) and SAE Bench (Karvonen et al., 2025) to evaluate properties of SAE features. We aim for the needs of resource-constrained mechanistic interpretability research where efficiency and interpretability are in favor rather than top reconstruction performance, and 100M-820M token budgets are widely adopted (Bussmann et al., 2025; Kharlapenko et al., 2025; Heap et al., 2025; Mudide et al., 2025; Karvonen et al., 2025), so we choose 125M, 500M, 1B and 2B token budgets for the experiments.

Our experiments (see detailed setup in Appendices A and D) address three questions:

1. Does KronSAE maintain EV comparable to baseline SAEs under fixed compute?
2. Which design choices (nonlinearity, (m, n, h)) drive EV improvements?
3. How do these choices affect properties and interpretability of learned latents?

4.1 ABLATIONS

We employ the iso-FLOPs setup: for each KronSAE variant of dictionary size F we allocate the same amount of FLOPs as was spent for the training of TopK SAE for token budget T and same F .

Reconstruction performance. As indicated on Figure 1, KronSAE achieves on-par performance with TopK given lower number of trainable parameters and outperforms Matryoshka SAE. The performance gap narrows when increasing the dictionary size, which indicate the potential scalability of our method for large dictionaries. See also result on Gemma-2 2B model in Appendix A.3.

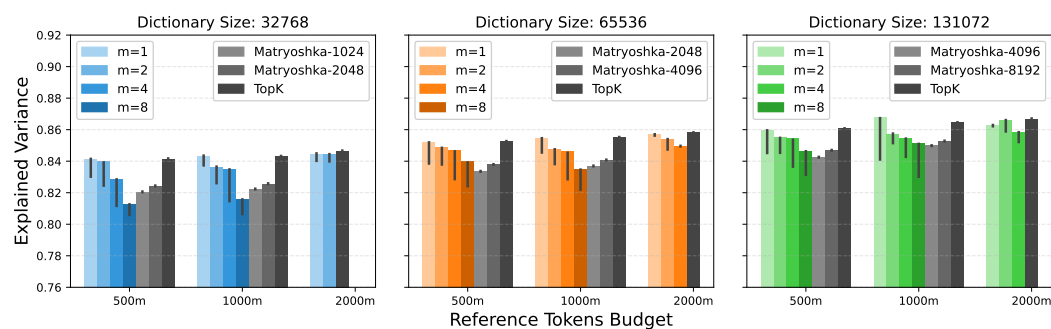
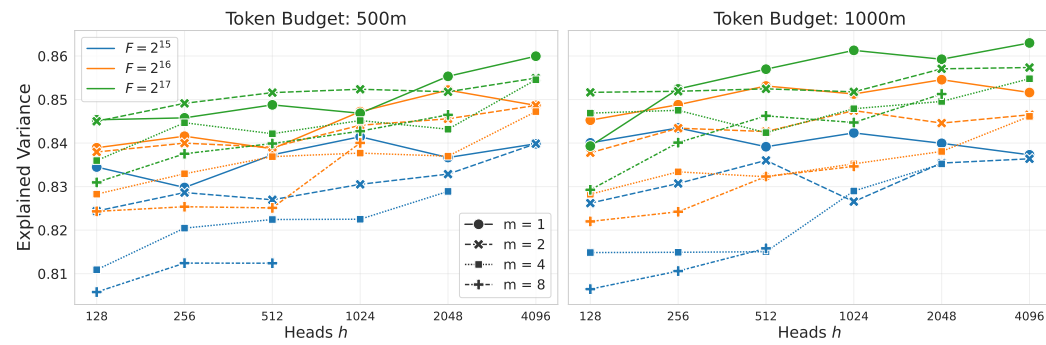


Figure 1: Maximum performance for KronSAE vs. TopK SAE vs. Matryoshka TopK SAE on Qwen-1.5B for different dictionary sizes F and budgets in iso-FLOP setting. KronSAE with lower number of parameters is on-par with the baseline, and the gap narrows with larger dictionary size.

162
 163 **Decomposition hyperparameters.** We systematically vary the number of heads h and the per-head
 164 base dimension m (with $n = F/(mh)$) under the iso-FLOPs setup. From the Figure 2, we conclude
 165 that lower m and higher h consistently yields higher reconstruction quality, due to flexibility of
 166 pre-latents - as we show in section 5.3, they must be either expressive or fine-grained enough (low m ,
 167 n and high h) to efficiently represent the semantics. See also Appendices A.5 and A.8.



178
 179 Figure 2: Dependency of EV on head count h (on the x-axis) and base dimension m under 500M and
 180 1B token budgets in iso-FLOPs setup. Higher h and smaller m yield improved reconstruction quality
 181 because of higher expressivity of pre-latents to encode semantics and increasing trainable parameters.
 182

183
 184 **Composition activation.** To isolate the impact of our mAND operator, we compare it to two
 185 simpler interaction kernels: (i) the element-wise product of ReLUs, $\text{ReLU}(u) \cdot \text{ReLU}(v)$, and (ii) the
 186 raw product $u \cdot v$. As reported in Table 1, under a 125M training budget, the mAND variant achieves
 187 the highest explained variance. More description of the mAND is provided in the Appendix C. See
 188 also our experiments where we replace TopK with JumpReLU in Appendix A.6.

Dictionary size	m	n	h	Activation	Explained Variance
32768	2	4	4096	$\text{mAND}(u, v)$	0.8336
				$\text{ReLU}(u) \cdot \text{ReLU}(v)$	0.8267
				$u \cdot v$	0.8237
	4	8	1024	$\text{mAND}(u, v)$	0.8220
				$\text{ReLU}(u) \cdot \text{ReLU}(v)$	0.8191
				$u \cdot v$	0.8143
65536	2	4	8192	$\text{mAND}(u, v)$	0.8445
				$\text{ReLU}(u) \cdot \text{ReLU}(v)$	0.8328
	4	8	2048	$\text{mAND}(u, v)$	0.8350
				$\text{ReLU}(u) \cdot \text{ReLU}(v)$	0.8297
				$u \cdot v$	0.8251

204 Table 1: Performance of different composition activations under a budget of 125M tokens.
 205

206 **Sparsity Analysis.** To evaluate performance across different sparsity budgets ($\ell_0 =$
 207 $\{16, 32, 64, 128\}$), we compare multiple SAE baselines (TopK SAE, Matryoshka SAE, Switch
 208 SAE) against their KronSAE variants at dictionary size $F = 2^{16}$ trained on 500 million tokens, under
 209 an iso-FLOPs budget matched to the TopK baseline. As shown in Figure 3, KronSAE achieves
 210 comparable reconstruction fidelity (measured by explained variance) to all baseline methods across
 211 all sparsity levels. Results for smaller dictionary size $F = 2^{15}$ are presented in Appendix A.4.
 212

213 **Layerwise performance.** Additionally, we evaluate performance across different layers in Qwen-
 214 2.5-1.5B. In every case, KronSAE matches the reconstruction quality of the TopK baseline, demon-
 215 strating that our Kronecker-factorized encoder maintains its performance regardless of depth. This
 setup and corresponding results are described in greater detail in Appendix A.6.

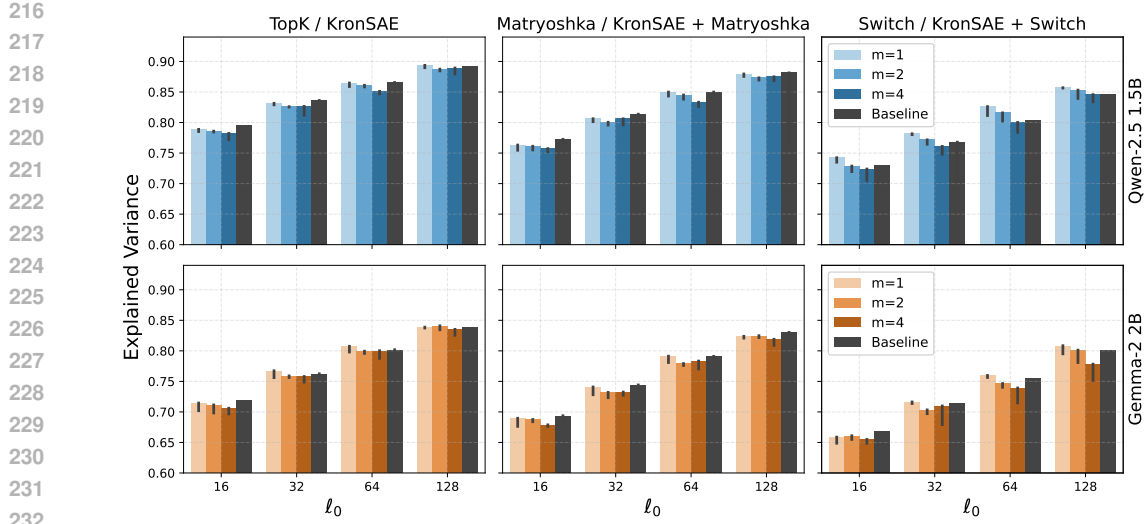


Figure 3: Maximum performance for baselines and their KronSAE modifications for different sparsity levels in iso-FLOP setting. KronSAE variants, despite using fewer trainable parameters, achieve reconstruction quality comparable to or better than the unmodified baselines.

4.2 ABSORPTION

The notorious challenge in SAE interpretability is *feature absorption*, where one learned feature becomes a strict subset of another and consequently fails to activate on instances that satisfy the broader concept but not its superset representation (e.g. a “starts with L” feature is entirely subsumed by a “Lion” feature) (Chanin et al., 2024).

Figure 4 reports three absorption metrics measured via SAEBench (Karvonen et al., 2025) across sparsity levels $\ell_0 \in \{16, 32, 64, 128\}$: (1) the *mean absorption fraction*, measuring the proportion of features that are partially absorbed; (2) the *mean full-absorption score*, quantifying complete subsumption events; and (3) the *mean number of feature splits*, indicating how often a single conceptual feature fragments into multiple activations. We use with dictionary size $F = 2^{16}$ and compare TopK SAE, Matryoshka SAE (Bussmann et al., 2025), and their KronSAE version, since they impose different hierarchical priors (see Appendix C for a discussion of how Matryshka SAE and TopK SAE structure differs). Across all ℓ_0 , KronSAE variants consistently reduce first two scores relative to the TopK SAE baseline, while maintaining a similar rate of feature splits.

We attribute KronSAE’s improved disentanglement to two complementary design choices:

1. **AND-like behaviour.** By ensuring that post-latent emits only when its more general pre-latent parents are active, we prevent more specific post-latents from entirely subsuming broadly polysemantic one. See additional description of this mechanism in Appendix C.
2. **Head-wise Cartesian decomposition.** Dividing the latent space into h independent subspaces (each with its own $m \times n$ grid of primitive interactions) ensures that specialized concepts (such as “elephant”) are confined to a single head and cannot fully absorb more general concepts (such as “starts with E”) in another.

Together, these mechanisms produce more monosemantic features, as we verify in the section 5.3, simplifying downstream applications. See results with dictionary size $F = 2^{15}$ in Appendix A.4. We also validate the result on Pythia models and observe the same picture, see the Appendix A.5.

5 ANALYSIS

In this section we examine the properties of the latents in KronSAE compared to TopK architecture.

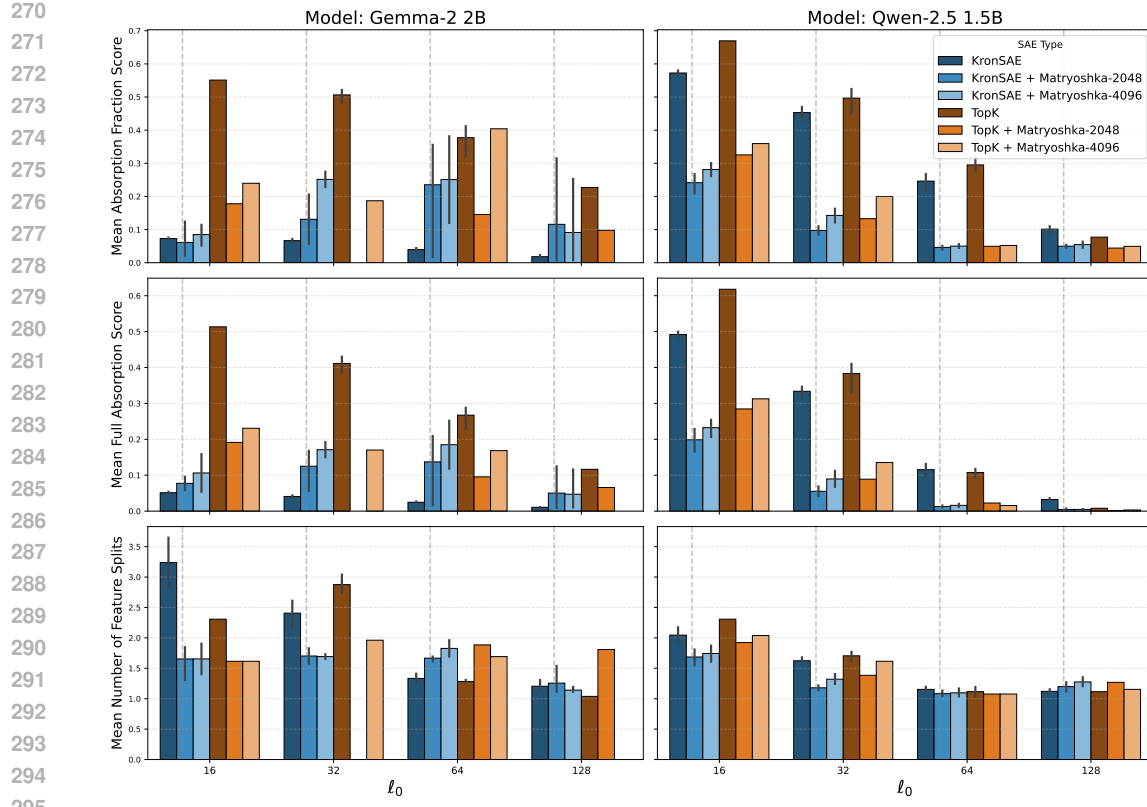


Figure 4: Feature absorption metrics on Qwen-2.5 1.5B and Gemma-2 2B. KronSAE configurations (various m, n) exhibit lower mean absorption fractions and full-absorption scores across different ℓ_0 and selected baselines.

The design of our architecture was also inspired by the observation that many features within a single SAE correlate with each other. **KronSAE introduces structural bias that forces the post-latents to co-occur with their pre-latents** (see also Appendix C). In this section we analyse if it is helpful.

By examining the toy examples with manufactured correlations in data, we show that KronSAE captures these correlations better than TopK. Then we show that KronSAE trained on language indeed moves correlated features within a single head, indicated by higher correlation within head. After that, we show that KronSAE pre-latents interactions are closely resemble the logic AND gate, and its post-latents are notably more interpretable than TopK latents.

5.1 TOY MODEL OF CORRELATION

To evaluate how well different sparse autoencoder architectures recover underlying correlation patterns, we construct a controlled experiment using a synthetic, block-structured covariance model. Input vectors $\mathbf{x} \in \mathbb{R}^F$ sampled from a normal distribution (with $\mu = 0, \sigma = 1$). We then perform a Cholesky decomposition $S = LL^\top$ on the covariance matrix S and set $\bar{\mathbf{x}}_{\text{sparse}} = L \text{TopK}(\text{ReLU}(\mathbf{x}))$, so that $\bar{\mathbf{x}}_{\text{sparse}}$ exhibits the desired structure.

We train autoencoder (AE) to reconstruct $\bar{\mathbf{x}}_{\text{sparse}}$ following the (Elhage et al., 2022):

$$\hat{\mathbf{x}} = \text{ReLU}(W^\top W \cdot \bar{\mathbf{x}}_{\text{sparse}} + \mathbf{b}). \quad (5)$$

We collect hidden states of dimension $d = 64$ ($W \cdot \bar{\mathbf{x}}_{\text{sparse}}$) from AE and then train TopK SAE and our proposed KronSAE with $F = 256$ and $\text{topk} = 8$ to reconstruct it. After training, we extract the decoder weight matrices W_{dec} from each SAE, match its latents with the autoencoder latents by **solving the quadratic assignment problem** (Vogelstein et al., 2015) (see Appendix B for motivation and details), and compute the covariance $C_{\text{dec}} = W_{\text{dec}} W_{\text{dec}}^\top$. Result is shown in Figure 5.

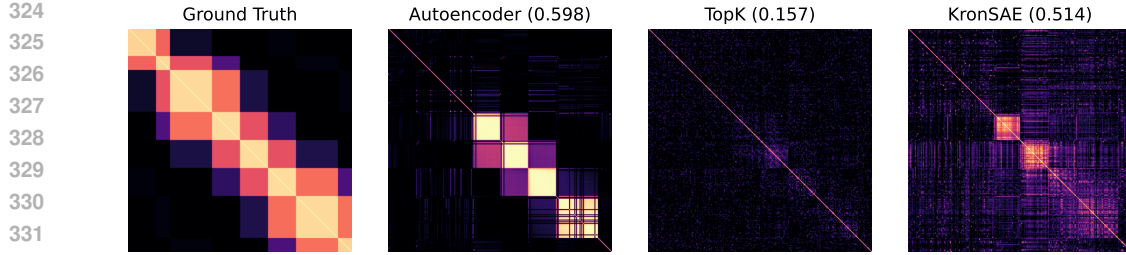


Figure 5: We generate data with covariance matrix that consist of blocks with different sizes on diagonal and off diagonal (left panel). We then examine the decoder-weight covariance $W_{\text{dec}} \cdot W_{\text{dec}}^T$ to assess feature-embedding correlations and compute the RV score to quantify the similarity between learned and ground truth covariance matrices. Second panel show feature embeddings for trained autoencoder $W_{\text{enc}} \cdot W_{\text{enc}}^T$. Third panel demonstrates that a TopK SAE recovers these correlation structures weakly, as indicated by relatively low RV coefficient (0.157) even after optimal atom matching. In contrast, KronSAE (right panel) more accurately reveals the original block patterns.

To quantify how closely each model’s feature correlations mirror the original structure of S , we employ the RV coefficient, defined as $RV(S, C) = \text{trace}(SC)/\sqrt{\text{trace}(S^2) \text{trace}(C^2)}$. In our experiments, KronSAE consistently achieves notably higher RV than TopK SAE, indicating that our compositional encoder more faithfully reconstructs the original feature relation. See also additional experiments in section B, where we provide further empirical intuition for how KronSAE identifies correlation structure that more closely align with those present in the data.

5.2 CORRELATIONS IN SAEs TRAINED ON LANGUAGE

To examine the correlation structure of features learned in our SAE, we have calculated the correlations on 5k texts from the training dataset. For each feature we calculate the mean correlation with features within its head and with all other features, and compare the randomly initialized KronSAE with $m = 4, n = 4$ with the trained one. To isolate the effect of our initialization procedure, we initialize the weights of SAE from the uniform distribution. As shown in Figure 6, correlations are indeed significantly higher within a single head and higher than for random SAE, which suggest that our choice to impose the correlated structure in SAE latents works as intended.

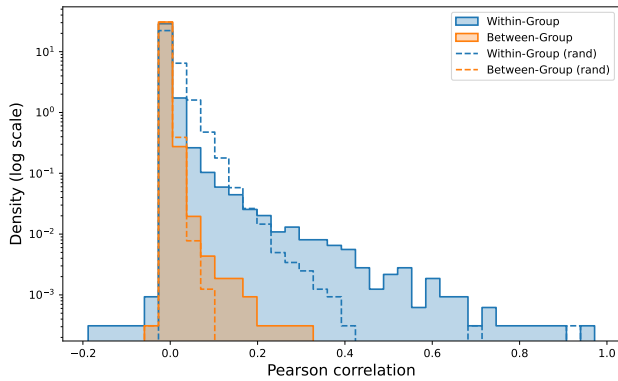


Figure 6: Correlations between features in KronSAE with $m = 4, n = 4$ within a head and with features from other heads. Our design induces higher correlations within a group, which also gets stronger after training, although SAE have also learned correlated features from different heads.

5.3 ANALYSIS OF LEARNED FEATURES

In this section we compare KronSAE and TopK SAE in terms of interpretability and feature properties, and we analyze the properties of groups in KronSAE. For this, we choose the 14th layer of Qwen2.5-

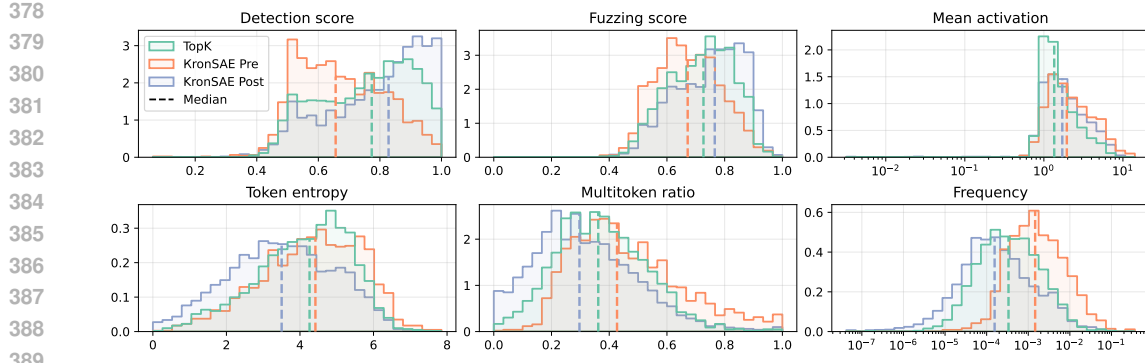


Figure 7: Distribution of properties for TopK SAE and KronSAE ($m = 4, n = 4$) with 32k dictionary size trained on Qwen2.5-1.5B. Pre and Post suffixes denote pre- and post- latents, and y-axis indicate density. **Token entropy** shows the entropy of the distribution of tokens on which feature has activated, and the **multitoken ratio** measures how often does feature activate in a single sequence. Our SAE achieves better interpretability scores by learning specialized feature groups, indicated by lower activation frequency and lower variance in activated tokens.

1.5B and a dictionary size of 32k features, of which the first 3072 were selected. KronSAE was chosen with $m = 4, n = 4$. We run for 24M tokens total to collect data. Our interpretation pipeline follows the common methodology: LLM interprets the activation patterns (Bills et al., 2023) and we evaluate obtained interpretations using the *detection score* and the *fuzzing score* Paulo et al. (2024).

For each selected feature, among the standard mean activation value and frequency, we calculate two additional metrics. Low values of *token entropy* suggest that feature activates more frequently on small number of tokens, thus it is token-specific; high value of *multitoken ratio* indicates that feature tends to activate multiple times in a single sentence. We have observed that both these metrics have notable negative correlation with the final interpretability scores and therefore they provide useful signal to assess the potential score without calculating it.

For more details on the data collection and interpretation pipeline, see Appendix D. For additional analysis of properties of learned features, **additional comparison with baselines and discussion about tradeoff between reconstruction performance and interpretability**, see Appendix E.

SAE properties and encoding mechanism. We observe that the features learned by KronSAE are more specific, indicated by lower values of the computed metrics and higher interpretability scores, as shown in Figure 7. Since post-latents are significantly more interpretable than corresponding pre-latents, we hypothesize the hidden mechanism for encoding and retrieval of the required semantics.

By examining activating examples and interpretations of latents, we observe that pre-latents may carry multiple distinct and identifiable modes of activation, such as composition base element 3 in head 23 shown in Table 2, and be very abstract compared to resulting post-latents. Polysemy of pre-latents is expected to be a consequence of reduced "working" number of encoder latents, since we decompose the full dictionary size and reduce the encoder capacity.

Thus, we hypothesize that the encoding of specific semantics in our SAE may be done via magnitude, which we validate by examining the activation examples. For the above mentioned pre-latent, the "comparison" part is encoded in the top 75% quantile, while the "spiritual" part is mostly met in the top 25% quantile, and the "geographical" part is mainly encoded in the interquartile range. We also consider but do not investigate the possibility that it may depend on the context, e.g. when the model uses the same linear direction to encode different concepts when different texts are passed to it.

Semantic retrieval and interpretable interactions. Heads usually contain a groups of semantically related pre-latents, e.g. in head 136 there are three base elements and one extension covering numbers and ordinality, two extension elements related to geographical and spatial matters, one question-related base and one growth-related extension. Interestingly, most post-latents for this head have higher interpretability score than both its parent pre-latents, which is unusual.

432 The retrieval happens primarily via the mechanism closely resembling the logical AND circuit, where
 433 some pre-latent works as the bearer of multiple semantics, and the corresponding pre-latent (base
 434 or extension) works as specifier. An illustrative example is shown in Table 2: we see that the base
 435 contains three detectable sub-semantics, and each extension then retrieves the particular semantics.
 436

Component	Interpretation	Score
Base 3	Suffix “-like” for comparative descriptors, directional terms indicating geographical regions, and concepts related to spiritual or metaphysical dimensions	0.84
Extension elements and their compositions with base 3		
Extension 0	<i>Interpretation:</i> Comparative expressions involving “than” and “as” in contrastive or proportional relationships.	0.87
	<i>Composition:</i> Similarity or analogy through the suffix “-like” across diverse contexts.	0.89
Extension 1	<i>Interpretation:</i> Specific terms, names, and abbreviations that are contextually salient and uniquely identifiable.	0.66
	<i>Composition:</i> Medical terminology related to steroids, hormones, and their derivatives.	0.84
Extension 2	<i>Interpretation:</i> Spiritual concepts and the conjunction “as” in varied syntactic roles.	0.80
	<i>Composition:</i> Abstract concepts tied to spirituality, consciousness, and metaphysical essence.	0.93
Extension 3	<i>Interpretation:</i> Directional and regional descriptors indicating geographical locations or cultural contexts.	0.84
	<i>Composition:</i> Directional terms indicating geographical or regional divisions.	0.91

462 Table 2: Interactions between composition base element 3 in head 23 and all extension elements in
 463 that head. Interaction happens in a way that closely resembles the Boolean AND operation: base
 464 pre-latent is polysemous, and the composition post-latent is the intersection, i.e. logical AND between
 465 parent pre-latents. See details in Section 5.3.

466
 467
 468 Other types of interaction may occur, such as appearance of completely new semantics, for example
 469 composition between base 3 and extension 1 in Table 2 where medical terminology arises and could
 470 not be interpreted as simple intersection between two pre-latents semantics. Another example is
 471 a case of head 3 where base 3 has sub-semantics related to technical instruments and extension 2
 472 have semantics related to the posession and necessity, and their combination gives the therapy and
 473 treatment semantics which looks more like addition than intersection.

474 It is a frequent case that post-latent inherit semantics of only one parent, or the impact of another
 475 parent is not detectable, which usually happens if parent has a very broad interpretation and low score.
 476 However, it requires more sophisticated techniques to properly identify the fine-grained structure
 477 of interactions than just looking at the resulting latent descriptions, so we leave it to further work.
 478 Despite this, the AND-like gate is a very common behavior. See more examples in Appendix G.

479
 480
 481 **Geometry of post-latents.** Each post-latent vector has a vector representation in the residual stream
 482 represented by the corresponding column in W_{dec} , which is the approximation of overcomplete basis
 483 vectors we search for when training SAEs. Our architectural design leads to clustering of feature
 484 embeddings so that post-latents produced by same head, base or a extension elements are grouped
 485 in a tight cluster, and the geometry is dependent on hyperparameters h, m, n we choose, which is
 expected and may be useful for further applications such as steering. See more details in Appendix E.

486 6 CONCLUSION AND FUTURE WORK

488 We introduce **KronSAE**, a sparse autoencoder architecture design that combines head-wise Kronecker
 489 factorization of latent space with a approximation of logical AND via mAND nonlinearity. Our
 490 approach allows to efficiently train interpretable and compositional SAE, especially in settings with
 491 limited compute budget or training data, while maintaining reconstruction fidelity and yielding
 492 more interpretable features by utilizing their correlations. Our analysis links these gains to the
 493 complementary effects of compositional latent structure and logical AND-style interactions, offering
 494 a new lens on how sparsity and factorization can synergise in representation learning.

495 **Limitations.** KronSAE introduces tradeoff between interpretability, efficiency and reconstruction
 496 performance, and due to reduced number of trainable parameters it is expected to lag behind TopK
 497 SAE at large budgets. Our evaluation is limited to mid-sized transformer models and moderate
 498 dictionary sizes; however, the main bottleneck there might be not the SAE itself, but the infrastructure
 499 required to handle these setups and the model inference.

500 **Future Work.** We identify three directions for extending this work: (i) *Transcoding*. Treat
 501 transcoders (Dunefsky et al., 2024) as implicit routers of information and investigate alternative
 502 logical gating functions (e.g. XOR or composite gates) to improve interpretability and circuit analysis.
 503 (ii) *Crosscoding*. Generalize KronSAE to a crosscoder setting (Lindsey et al., 2024) uncover
 504 interpretable, cross-level compositionality via logic operations. (iii) *Dynamic Composition*. Explore
 505 learnable tuning of both the number of attention heads and their dimensionality, enabling fine-grained
 506 decomposition into groups of correlated features at varying scales.

509 ETHICS STATEMENT

511 While interpretability research has dual-use potential, our method operates within the ethical bound-
 512 aries of the underlying models and aims to advance responsible AI development through better model
 513 understanding. We analyze activations from publicly available language models (Qwen-2.5-1.5B,
 514 Pythia-1.4B, and Gemma-2-2B) gathered on FineWeb-Edu datasets, which excludes the unreported
 515 harmful content. We declare no conflicts of interest and maintain transparency about limitations,
 516 including potential artifacts from LLM-based interpretation as noted in Appendices D.3 and I.

518 REPRODUCIBILITY STATEMENT

520 We have taken several measures to ensure the reproducibility of our results. We use publicly available
 521 models (Qwen, Gemma, Pythia families) and training dataset (FineWeb-Edu) in our experiments.
 522 Section 4 and Appendix A provide detailed description of SAE training procedure and hyperparameter
 523 configuration. Our complete implementation is available in the supplementary materials, containing
 524 the training code, interpretation pipeline and analysis of the results. Appendix H includes simplified
 525 implementation of KronSAE that might be easily integrated into existing training codebases, while
 526 Appendix D details the interpretability analysis methodology with precise evaluation protocols.

528 REFERENCES

529 Nikita Balagansky, Ian Maksimov, and Daniil Gavrilov. Mechanistic permutability: Match features
 530 across layers. In *The Thirteenth International Conference on Learning Representations*, 2025.
 531 URL <https://openreview.net/forum?id=MDvecs7Evo>.

532 Stella Biderman, Hailey Schoelkopf, Quentin Anthony, Herbie Bradley, Kyle O'Brien, Eric Hallahan,
 533 Mohammad Aflah Khan, Shivanshu Purohit, USVSN Sai Prashanth, Edward Raff, Aviya Skowron,
 534 Lintang Sutawika, and Oskar van der Wal. Pythia: A suite for analyzing large language models
 535 across training and scaling, 2023. URL <https://arxiv.org/abs/2304.01373>.

537 Steven Bills, Nick Cammarata, Dan Mossing, Henk Tillman, Leo Gao, Gabriel Goh,
 538 Ilya Sutskever, Jan Leike, Jeff Wu, and William Saunders. Language models can
 539 explain neurons in language models, 2023. URL <https://openai.com/index/language-models-can-explain-neurons-in-language-models/>.

540 Trenton Bricken, Adly Templeton, Joshua Batson, Brian Chen, Adam Jermyn, Tom Conerly, Nick
 541 Turner, Cem Anil, Carson Denison, Amanda Askell, et al. Towards monosemanticity: Decompos-
 542 ing language models with dictionary learning. *Transformer Circuits Thread*, 2, 2023.

543

544 Bart Bussmann, Noa Nabeshima, Adam Karvonen, and Neel Nanda. Learning multi-level features
 545 with matryoshka sparse autoencoders. In *Forty-second International Conference on Machine
 546 Learning*, 2025. URL <https://openreview.net/forum?id=m25T5rAy43>.

547 David Chanin, James Wilken-Smith, Tomáš Dulka, Hardik Bhatnagar, and Joseph Bloom. A is
 548 for absorption: Studying feature splitting and absorption in sparse autoencoders, 2024. URL
 549 <https://arxiv.org/abs/2409.14507>.

550

551 Hoagy Cunningham, Aidan Ewart, Logan Riggs, Robert Huben, and Lee Sharkey. Sparse autoen-
 552 coders find highly interpretable features in language models. In *International Conference on
 553 Learning Representations (ICLR)*, 2024. URL <https://openreview.net/forum?id=F76bwRSLeK>.

554

555 Tri Dao, Beidi Chen, Nimit Sharad Sohoni, Arjun D. Desai, Michael Poli, Jessica Grogan, Alexander
 556 Liu, Aniruddh Rao, Atri Rudra, and Christopher Ré. Monarch: Expressive structured matrices for
 557 efficient and accurate training. In *ICML*, pp. 4690–4721, 2022. URL <https://proceedings.mlr.press/v162/dao22a.html>.

558

559 Jacob Dunefsky, Philippe Chlenski, and Neel Nanda. Transcoders find interpretable LLM feature
 560 circuits. In *The Thirty-eighth Annual Conference on Neural Information Processing Systems*, 2024.
 561 URL <https://openreview.net/forum?id=J6zHcScAo0>.

562

563 Ali Edalati, Marzieh Tahaei, Ahmad Rashid, Vahid Partovi Nia, James J. Clark, and Mehdi Reza-
 564 gholizadeh. Kronecker decomposition for gpt compression, 2021. URL <https://arxiv.org/abs/2110.08152>.

565

566 Nelson Elhage, Tristan Hume, Catherine Olsson, Nicholas Schiefer, Tom Henigan, Shauna Kravec,
 567 Zac Hatfield-Dodds, Robert Lasenby, Dawn Drain, Carol Chen, Roger Grosse, Sam McCandlish,
 568 Jared Kaplan, Dario Amodei, Martin Wattenberg, and Christopher Olah. Toy models of superposi-
 569 tion. *Transformer Circuits Thread*, 2022. URL https://transformer-circuits.pub/2022/toy_model/index.html.

570

571 Nelson Elhage et al. Decomposing language models with dictionary learning. *Trans-
 572 former Circuits*, 2023. URL <https://transformer-circuits.pub/2023/monosemantic-features>.

573

574

575 Thomas Fel, Ekdeep Singh Lubana, Jacob S. Prince, Matthew Kowal, Victor Boutin, Isabel Pa-
 576 padimitriou, Bin Xu Wang, Martin Wattenberg, Demba E. Ba, and Talia Konkle. Archety-
 577 pal SAE: Adaptive and stable dictionary learning for concept extraction in large vision mod-
 578 els. In *Forty-second International Conference on Machine Learning*, 2025. URL <https://openreview.net/forum?id=9v1eW8HgMU>.

579

580 Leo Gao, Tom Dupre la Tour, Henk Tillman, Gabriel Goh, Rajan Troll, Alec Radford, Ilya Sutskever,
 581 Jan Leike, and Jeffrey Wu. Scaling and evaluating sparse autoencoders. In *The Thirteenth
 582 International Conference on Learning Representations*, 2025. URL <https://openreview.net/forum?id=tcsZt9ZNKD>.

583

584 Thomas Heap et al. Sparse autoencoders can interpret randomly initialized transformers. *arXiv
 585 preprint arXiv:2501.17727*, 2025. URL <https://arxiv.org/abs/2501.17727>.

586

587 Adam Karvonen, Can Rager, Johnny Lin, Curt Tigges, Joseph Bloom, David Chanin, Yeu-Tong Lau,
 588 Eoin Farrell, Callum McDougall, Kola Ayonrinde, Matthew Wearden, Arthur Conmy, Samuel
 589 Marks, and Neel Nanda. Saebench: A comprehensive benchmark for sparse autoencoders in
 590 language model interpretability, 2025. URL <https://arxiv.org/abs/2503.09532>.

591

592 Dmitrii Kharlapenko, Stepan Shabalin, Arthur Conmy, and Neel Nanda. Scaling sparse feature
 593 circuits for studying in-context learning. In *Sparsity in LLMs (SLLM): Deep Dive into Mixture of
 Experts, Quantization, Hardware, and Inference*, 2025. URL <https://openreview.net/forum?id=sdLwJTtKpM>.

594 Jack Lindsey, Adly Templeton, Jonathan Marcus, Thomas Conerly, Joshua Batson, and Christopher
 595 Olah. Sparse crosscoders for cross-layer features and model diffing, 2024. URL <https://transformer-circuits.pub/2024/crosscoders/index.html>.
 596

597 Scott C. Lowe et al. Logical activation functions: Logit-space equivalents of probabilistic boolean
 598 operators. *arXiv preprint arXiv:2110.11940*, 2021. URL <https://arxiv.org/abs/2110.11940>.
 599

600 Samuel Marks, Can Rager, Eric J Michaud, Yonatan Belinkov, David Bau, and Aaron Mueller.
 601 Sparse feature circuits: Discovering and editing interpretable causal graphs in language models.
 602 In *The Thirteenth International Conference on Learning Representations*, 2025. URL <https://openreview.net/forum?id=I4e82CIDxv>.
 603

604 Anish Mudide, Joshua Engels, Eric J Michaud, Max Tegmark, and Christian Schroeder de Witt.
 605 Efficient dictionary learning with switch sparse autoencoders. In *The Thirteenth International
 606 Conference on Learning Representations*, 2025. URL <https://openreview.net/forum?id=k2ZVAzVeMP>.
 607

608 Gonçalo Paulo and Nora Belrose. Sparse autoencoders trained on the same data learn different
 609 features, 2025. URL <https://arxiv.org/abs/2501.16615>.
 610

611 Gonçalo Paulo, Alex Mallen, Caden Juang, and Nora Belrose. Automatically interpreting millions of
 612 features in large language models, 2024. URL <https://arxiv.org/abs/2410.13928>.
 613

614 Guilherme Penedo, Hynek Kydlíček, Loubna Ben allal, Anton Lozhkov, Margaret Mitchell, Colin
 615 Raffel, Leandro Von Werra, and Thomas Wolf. The fineweb datasets: Decanting the web for the
 616 finest text data at scale, 2024. URL <https://arxiv.org/abs/2406.17557>.
 617

618 Senthooran Rajamanoharan, Arthur Conmy, Lewis Smith, Tom Lieberum, Vikrant
 619 Varma, János Kramár, Rohin Shah, and Neel Nanda. Improving sparse decomposition
 620 of language model activations with gated sparse autoencoders. In *NeurIPS*,
 621 2024a. URL http://papers.nips.cc/paper_files/paper/2024/hash/01772a8b0420baec00c4d59fe2fbace6-Abstract-Conference.html.
 622

623 Senthooran Rajamanoharan, Tom Lieberum, Nicolas Sonnerat, Arthur Conmy, Vikrant Varma, János
 624 Kramár, and Neel Nanda. Jumping ahead: Improving reconstruction fidelity with jumprelu sparse
 625 autoencoders, 2024b. URL <https://arxiv.org/abs/2407.14435>.
 626

627 Noam Shazeer, Azalia Mirhoseini, Krzysztof Maziarz, Andy Davis, Quoc V. Le, Geoffrey Hinton,
 628 and Jeff Dean. Outrageously large neural networks: The sparsely-gated mixture-of-experts
 629 layer. In *International Conference on Learning Representations (ICLR)*, 2017. URL <https://arxiv.org/abs/1701.06538>.
 630

631 P. Smolensky. Tensor product variable binding and the representation of symbolic structures in
 632 connectionist systems. *Artif. Intell.*, 46(1–2):159–216, November 1990. ISSN 0004-3702. doi:
 633 10.1016/0004-3702(90)90007-M. URL [https://doi.org/10.1016/0004-3702\(90\)90007-M](https://doi.org/10.1016/0004-3702(90)90007-M).
 634

635 Paul Smolensky, Roland Fernandez, Zhenghao Herbert Zhou, Mattia Opper, and Jianfeng Gao.
 636 Mechanisms of symbol processing for in-context learning in transformer networks, 2024. URL
 637 <https://arxiv.org/abs/2410.17498>.
 638

639 Paul Soulos, R. Thomas McCoy, Tal Linzen, and Paul Smolensky. Discovering the compositional
 640 structure of vector representations with role learning networks. In Afra Alishahi, Yonatan Belinkov,
 641 Grzegorz Chrupała, Dieuwke Hupkes, Yuval Pinter, and Hassan Sajjad (eds.), *Proceedings of the
 642 Third BlackboxNLP Workshop on Analyzing and Interpreting Neural Networks for NLP*, pp. 238–
 643 254, Online, November 2020. Association for Computational Linguistics. doi: 10.18653/v1/2020.
 644 blackboxnlp-1.23. URL <https://aclanthology.org/2020.blackboxnlp-1.23/>.
 645

646 Gemma Team, Morgane Riviere, Shreya Pathak, Pier Giuseppe Sessa, Cassidy Hardin, Surya
 647 Bhupatiraju, Léonard Hussonot, Thomas Mesnard, Bobak Shahriari, Alexandre Ramé, Johan
 Ferret, Peter Liu, Pouya Tafti, Abe Friesen, Michelle Casbon, Sabela Ramos, Ravin Kumar,
 Charline Le Lan, Sammy Jerome, Anton Tsitsulin, Nino Vieillard, Piotr Stanczyk, Sertan Girgin,

648 Nikola Momchev, Matt Hoffman, Shantanu Thakoor, Jean-Bastien Grill, Behnam Neyshabur,
 649 Olivier Bachem, Alanna Walton, Aliaksei Severyn, Alicia Parrish, Aliya Ahmad, Allen Hutchison,
 650 Alvin Abdagic, Amanda Carl, Amy Shen, Andy Brock, Andy Coenen, Anthony Laforge, Antonia
 651 Paterson, Ben Bastian, Bilal Piot, Bo Wu, Brandon Royal, Charlie Chen, Chintu Kumar, Chris
 652 Perry, Chris Welty, Christopher A. Choquette-Choo, Danila Sinopalnikov, David Weinberger,
 653 Dimple Vijaykumar, Dominika Rogozińska, Dustin Herbison, Elisa Bandy, Emma Wang, Eric
 654 Noland, Erica Moreira, Evan Senter, Evgenii Eltyshev, Francesco Visin, Gabriel Rasskin, Gary
 655 Wei, Glenn Cameron, Gus Martins, Hadi Hashemi, Hanna Klimczak-Plucińska, Harleen Batra,
 656 Harsh Dhand, Ivan Nardini, Jacinda Mein, Jack Zhou, James Svensson, Jeff Stanway, Jetha
 657 Chan, Jin Peng Zhou, Joana Carrasqueira, Joana Iljazi, Jocelyn Becker, Joe Fernandez, Joost
 658 van Amersfoort, Josh Gordon, Josh Lipschultz, Josh Newlan, Ju yeong Ji, Kareem Mohamed,
 659 Kartikeya Badola, Kat Black, Katie Millican, Keelin McDonell, Kelvin Nguyen, Kiranbir Sodhia,
 660 Kish Greene, Lars Lowe Sjoesund, Lauren Usui, Laurent Sifre, Lena Heuermann, Leticia Lago,
 661 Lilly McNealus, Livio Baldini Soares, Logan Kilpatrick, Lucas Dixon, Luciano Martins, Machel
 662 Reid, Manvinder Singh, Mark Iverson, Martin Görner, Mat Velloso, Mateo Wirth, Matt Davidow,
 663 Matt Miller, Matthew Rahtz, Matthew Watson, Meg Risdal, Mehran Kazemi, Michael Moynihan,
 664 Ming Zhang, Minsuk Kahng, Minwoo Park, Mofi Rahman, Mohit Khatwani, Natalie Dao, Nenshad
 665 Bardoliwalla, Nesh Devanathan, Neta Dumai, Nilay Chauhan, Oscar Wahltinez, Pankil Botarda,
 666 Parker Barnes, Paul Barham, Paul Michel, Pengchong Jin, Petko Georgiev, Phil Culliton, Pradeep
 667 Kuppala, Ramona Comanescu, Ramona Merhej, Reena Jana, Reza Ardeshir Rokni, Rishabh
 668 Agarwal, Ryan Mullins, Samaneh Saadat, Sara Mc Carthy, Sarah Cogan, Sarah Perrin, Sébastien
 669 M. R. Arnold, Sebastian Krause, Shengyang Dai, Shruti Garg, Shruti Sheth, Sue Ronstrom, Susan
 670 Chan, Timothy Jordan, Ting Yu, Tom Eccles, Tom Hennigan, Tomas Kociský, Tulsee Doshi,
 671 Vihan Jain, Vikas Yadav, Vilobh Meshram, Vishal Dharmadhikari, Warren Barkley, Wei Wei,
 672 Wenming Ye, Woohyun Han, Woosuk Kwon, Xiang Xu, Zhe Shen, Zhitao Gong, Zichuan Wei,
 673 Victor Cotrutz, Phoebe Kirk, Anand Rao, Minh Giang, Ludovic Peran, Tris Warkentin, Eli Collins,
 674 Joelle Barral, Zoubin Ghahramani, Raia Hadsell, D. Sculley, Jeanine Banks, Anca Dragan, Slav
 675 Petrov, Oriol Vinyals, Jeff Dean, Demis Hassabis, Koray Kavukcuoglu, Clement Farabet, Elena
 676 Buchatskaya, Sebastian Borgeaud, Noah Fiedel, Armand Joulin, Kathleen Kenealy, Robert Dadashi,
 677 and Alek Andreev. Gemma 2: Improving open language models at a practical size, 2024. URL
 678 <https://arxiv.org/abs/2408.00118>.

679 Adly Templeton, Tom Conerly, Jonathan Marcus, Jack Lindsey, Trenton Bricken, Brian Chen,
 680 Adam Pearce, Craig Citro, Emmanuel Ameisen, Andy Jones, Hoagy Cunningham, Nicholas L
 681 Turner, Callum McDougall, Monte MacDiarmid, C. Daniel Freeman, Theodore R. Sumers,
 682 Edward Rees, Joshua Batson, Adam Jermyn, Shan Carter, Chris Olah, and Tom Henighan.
 683 Scaling monosemanticity: Extracting interpretable features from claude 3 sonnet. *Transformer Circuits Thread*, 2024. URL <https://transformer-circuits.pub/2024/scaling-monosemanticity/index.html>.

684 Joshua T. Vogelstein, John M. Conroy, Vince Lyzinski, Louis J. Podrazik, Steven G. Kratzer,
 685 Eric T. Harley, Donniell E. Fishkind, R. Jacob Vogelstein, and Carey E. Priebe. Fast ap-
 686 proximate quadratic programming for graph matching. *PLoS ONE*, 10, 2015. URL <https://api.semanticscholar.org/CorpusID:16927142>.

687 Peihao Wang, Rameswar Panda, Lucas Torroba Hennigen, Philip Greengard, Leonid Karlinsky,
 688 Rogerio Feris, David Daniel Cox, Zhangyang Wang, and Yoon Kim. Learning to grow pretrained
 689 models for efficient transformer training. In *The Eleventh International Conference on Learning
 690 Representations*, 2023. URL <https://openreview.net/forum?id=cDYRS5iZ16f>.

691 An Yang, Baosong Yang, Beichen Zhang, Binyuan Hui, Bo Zheng, Bowen Yu, Chengyuan Li,
 692 Dayiheng Liu, Fei Huang, Haoran Wei, Huan Lin, Jian Yang, Jianhong Tu, Jianwei Zhang, Jianxin
 693 Yang, Jiaxi Yang, Jingren Zhou, Junyang Lin, Kai Dang, Keming Lu, Keqin Bao, Kexin Yang,
 694 Le Yu, Mei Li, Mingfeng Xue, Pei Zhang, Qin Zhu, Rui Men, Runji Lin, Tianhao Li, Tingyu Xia,
 695 Xingzhang Ren, Xuancheng Ren, Yang Fan, Yang Su, Yichang Zhang, Yu Wan, Yuqiong Liu, Zeyu
 696 Cui, Zhenru Zhang, and Zihan Qiu. Qwen2.5 technical report. *arXiv preprint arXiv:2412.15115*,
 697 2024.

698 An Yang, Anfeng Li, Baosong Yang, Beichen Zhang, Binyuan Hui, Bo Zheng, Bowen Yu, Chang
 699 Gao, Chengen Huang, Chenxu Lv, Chujie Zheng, Dayiheng Liu, Fan Zhou, Fei Huang, Feng Hu,

702 Hao Ge, Haoran Wei, Huan Lin, Jialong Tang, Jian Yang, Jianhong Tu, Jianwei Zhang, Jianxin
703 Yang, Jiaxi Yang, Jing Zhou, Jingren Zhou, Junyang Lin, Kai Dang, Keqin Bao, Kexin Yang,
704 Le Yu, Lianghao Deng, Mei Li, Mingfeng Xue, Mingze Li, Pei Zhang, Peng Wang, Qin Zhu, Rui
705 Men, Ruize Gao, Shixuan Liu, Shuang Luo, Tianhao Li, Tianyi Tang, Wenbiao Yin, Xingzhang
706 Ren, Xinyu Wang, Xinyu Zhang, Xuancheng Ren, Yang Fan, Yang Su, Yichang Zhang, Yinger
707 Zhang, Yu Wan, Yuqiong Liu, Zekun Wang, Zeyu Cui, Zhenru Zhang, Zhipeng Zhou, and Zihan
708 Qiu. Qwen3 technical report, 2025. URL <https://arxiv.org/abs/2505.09388>.

709

710

711

712

713

714

715

716

717

718

719

720

721

722

723

724

725

726

727

728

729

730

731

732

733

734

735

736

737

738

739

740

741

742

743

744

745

746

747

748

749

750

751

752

753

754

755

756 A ADDITIONAL DETAILS AND RESULTS
757758 A.1 EXPERIMENTAL SETUP
759

760 **Training details.** All SAEs are optimized using AdamW with an initial learning rate of 8×10^{-4} ,
761 a cosine learning-rate schedule with a minimum LR of 1×10^{-6} , and a linear warmup for the first
762 10% of total training steps, auxiliary loss penalty equal to 0.03125. We use a global batch size of
763 8,192. We sweep over dictionary (latent) sizes of $F = 2^{15}$, $F = 2^{16}$, and $F = 2^{17}$ features. For
764 our KronSAE variant, we further sweep the number of heads h and the per-head dimensions m and
765 n such that $h \cdot m \cdot n$ equals the desired dictionary size. Regularization weights and auxiliary loss
766 coefficients are kept constant throughout the runs to isolate the impact of architectural choices.
767

768 For all experiments, we spent about 330 GPU days on NVIDIA H100 80GB GPUs, including
769 preliminary research.
770

771 **SAE.** For all experiments on Qwen-2.5, we train each SAE on activations from layer 14. Also for
772 Pythia-1.4B we use layer 14 and for Gemma-2-2B we take activations from layer 12. For most of our
773 experiments, we use sparsity level of $\ell_0 = 50$ non-zero activations per token.
774

775 **Initialization.** As observed by Gao et al. (2025), initializing the decoder as the transpose of the
776 encoder ($W_{\text{dec}} = W_{\text{enc}}^\top$) provides a strong metric improvement. We adopt this strategy within
777 KronSAE by partitioning W_{enc} into h head-wise blocks of shapes $m \times d$ and $n \times d$, denoted
778 $\{P_i, Q_i\}_{i=1}^h$. For each head k , we define its decoded rows via a simple additive composition:
779

$$C_k[i, j] = P_{k,i} + Q_{k,j}, \quad i = 1, \dots, m, \quad j = 1, \dots, n.$$

780 Finally, flattening the matrices $\{C_k\}$ yields full decoder weight matrix $W_{\text{dec}} \in \mathbb{R}^{F \times d}$.
781

782 **Matryoshka and Kron-based version.** For Matryoshka SAE of dictionary size F we adopt the fol-
783 lowing experimental setup. We use most training settings from Training details. For Matryoshka SAE
784 Bussmann et al. (2025) we define the parameter of dictionary group $S = [2^k, 2^k, \dots, 2^{k+i}, \dots, 2^n]$,
785 where $k < n$ and $\sum_{s \in S} s = F$. This is equivalent to nested sub-SAEs with dictionary sizes
786 $\mathcal{M} = \{2^k, 2^k + 2^k, 2^k + 2^k + 2^{k+1}, \dots, F\}$ and in our work we define this SAE as **Matryoshka-2^k**.
787 Training loss for Matryoshka is defined as follows:

$$\mathcal{L}(\mathbf{f}) = \sum_{m \in \mathcal{M}} \|\mathbf{x} - \mathbf{f}_{0:m} W_{0:m}^{\text{dec}} + b_{\text{dec}}\|_2^2 + \alpha \mathcal{L}_{\text{aux}}, \quad (6)$$

788 where \mathbf{f} is latent vector and \mathcal{L}_{aux} is auxiliary loss used in Gao et al. (2025).
789

790 For Kron-based Matryoshka SAE we use same setup and same initialization from Initialization
791 section. We choose m and n so that $F \bmod mn = 0$, ensuring that no heads are shared between
792 groups.
793

794 **Switch SAE and Kron-based version.** For the Switch SAE architecture proposed by Mudide et al.
795 (2025), we configure all experiments with 8 experts and use identical initialization from KronSAE. In
796 the Kron-based variant of this SAE, we distribute the heads equally across all experts, resulting in
797 $F/(8mn)$ heads per expert. Hence we have less parameters in every expert and therefore we also
798 reduce FLOPs for encoder.
799

800 A.2 FLOPS CALCULATION AND EFFICIENCY
801

802 For TopK SAE and KronSAE we compute FLOPs in the following way:
803

$$\begin{aligned} \text{FLOPS}_{\text{TopK}}(d, F, k) &= dF + kd, \\ \text{FLOPS}_{\text{KronSAE}}(d, m, n, h, k) &= dh(m + n) + mnh + kd \approx dh(m + n) + kd. \end{aligned} \quad (7)$$

804 We calculate FLOPs for most effective variant of TopK where we perform vector matrix multiplication
805 only for nonzero activations, while encoder still requires dense matrix multiplication.
806

We have also measured the wallclock time for forward and backward to examine the scaling. Figure 8 reports scaling for different hidden dimension sizes.

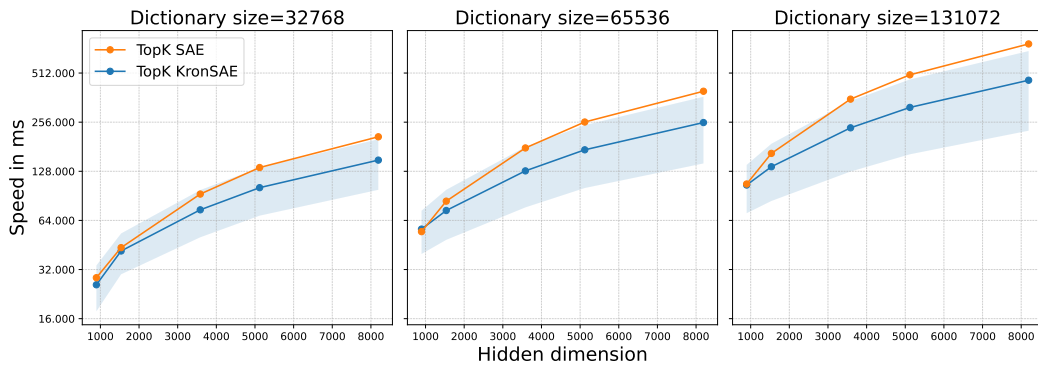


Figure 8: Speed comparision of TopK SAE with KronSAE across different hidden dimensionss. We can see that KronSAE have better scaling properties than SAE with default encoder architecture.

A.3 SCALING ON GEMMA-2 2B

To examine the method’s generality, we conducted additional reconstruction experiments on Gemma-2 2B under iso-FLOPs settings. As shown in Figure 9, our method achieves comparable or improved reconstruction performance across the evaluated compute budgets.

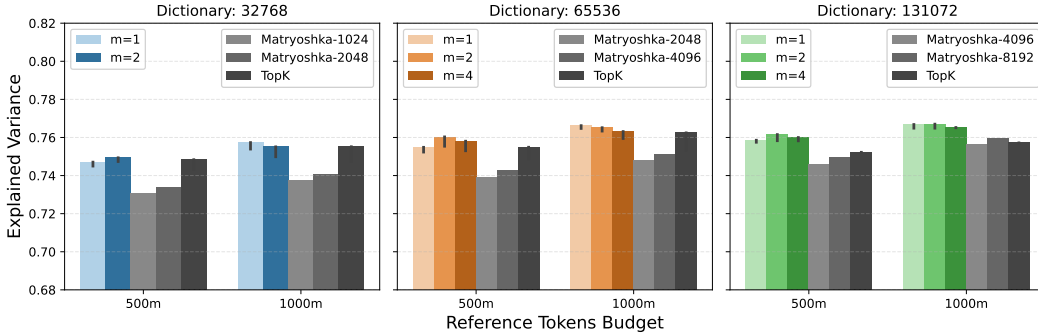


Figure 9: Performance comparision of KronSAE and TopK SAE under a fixed iso-FLOPs budget. Across sparsity settings, KronSAE typically matches TopK’s reconstruction performance and in some cases slightly outperforms it, while using much fewer trainable parameters.

A.4 SMALLER DICTIONARY SIZE

To complement our larger-scale experiments, we further evaluate KronSAE’s performance on a smaller dictionary size $F = 2^{15}$ with varying $\ell_0 = \{16, 32, 64, 128\}$ and **equal token budget**.

Sparsity. Following the experimental setup described in Section 4.1, we compare KronSAE against established baselines including TopK SAE, Matryoshka SAE, and Switch SAE . As shown in Figure 10, KronSAE consistently matches or exceeds the reconstruction performance of baseline architectures across all tested sparsity levels, while achieving these results with substantially fewer trainable parameters and FLOPs.

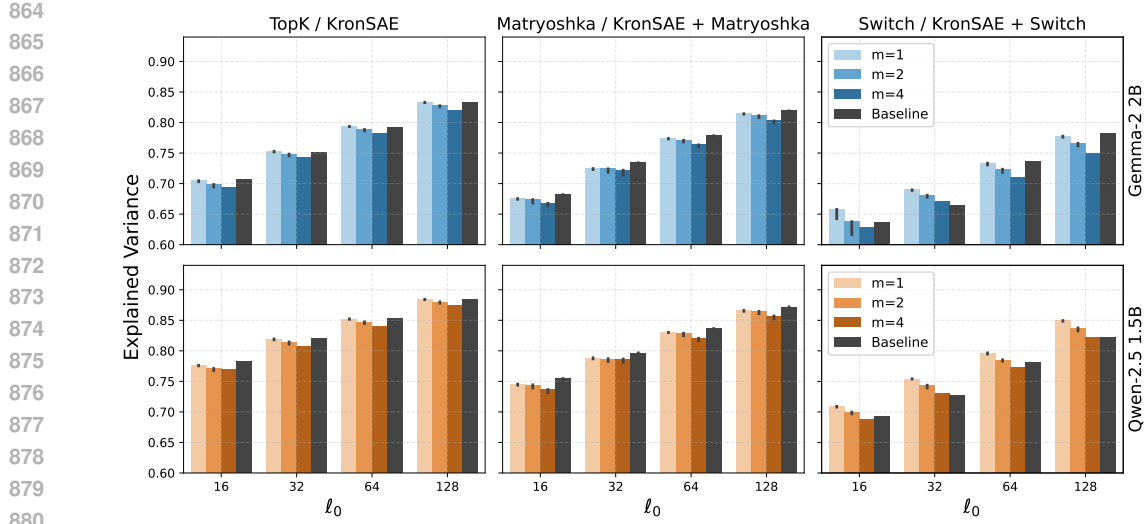


Figure 10: Performance comparison of KronSAE and TopK SAE under a fixed token budget. Across sparsity settings, KronSAE typically matches TopK’s reconstruction performance and in some cases slightly outperforms it, while using much fewer trainable parameters and smaller FLOPs budget.

Feature absorption. We extend our feature absorption analysis from Section 4.2 to the smaller dictionary size, employing two distinct grouping schedules: $S_1 = [2048, 2048, 4096, 8192, 16384]$ and $S_2 = [1024, 1024, 2048, 4096, 8192, 16384]$. As shown in Figure 11 KronSAE modification demonstrates better performance, reducing feature absorption metrics.

A.5 PYTHIA SUITE

For Pythia-1.4B we train all SAEs on the 12th transformer layer with a budget of 125M tokens. As reported in Table 3, KronSAE achieves performance comparable to TopK SAE with increased number of heads.

Dictionary	SAE	Mean	Max
32k	TopK	0.783	0.793
	KronSAE		0.793
65k	TopK	0.795	0.802
	KronSAE		0.805
131k	TopK	0.800	0.801
	KronSAE		0.810

Table 3: Performance of Pythia-1.4B at 125M budget. At larger dictionary size and fixed training budget KronSAE outperforms TopK SAE.

We conducted additional experiments with smaller Pythia models and trained KronSAE at the middle layers with 512 heads. Table 4 reports results for 125M budget on 65k and 262k dictionary sizes.

In section 4.2 we have analysed whether KronSAE achieves lower absorption score and have answered affirmatively. We also compare the results for Pythia 1.4B model and validate the improvements, as reported in the Table 5.

These results confirm that our compositional architectures improves the absorption score and feature consistency across various models from different families.

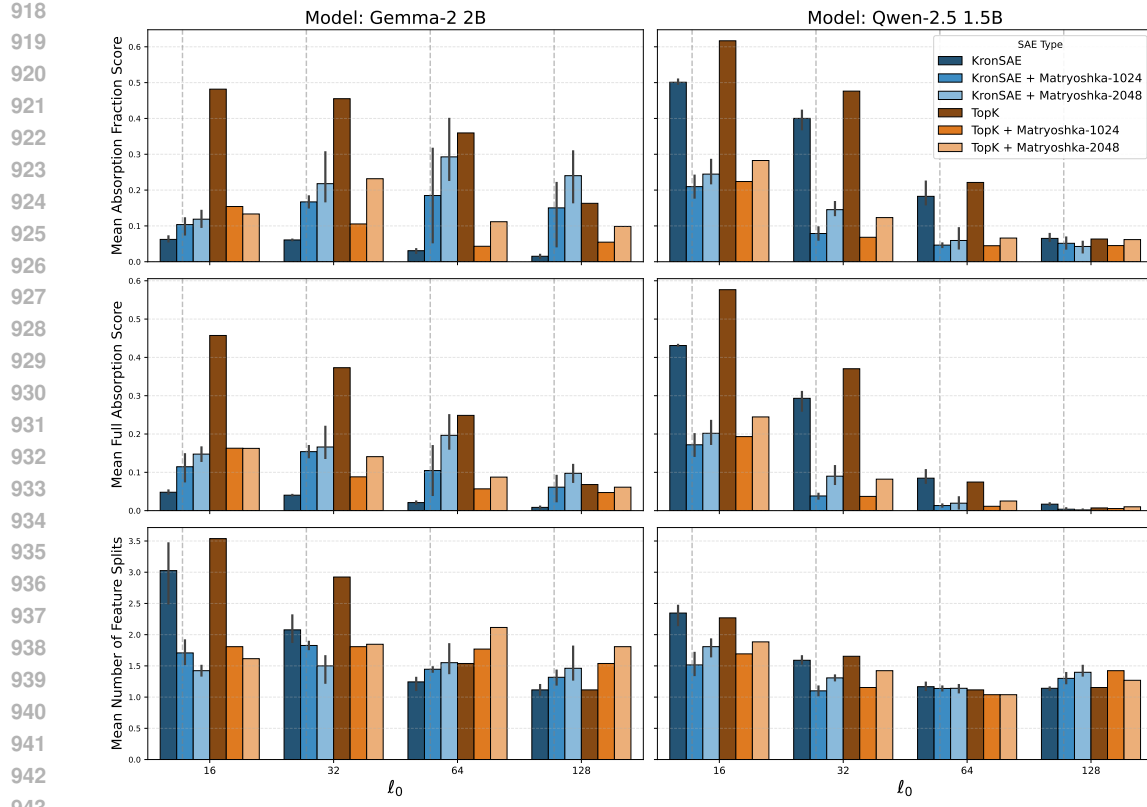


Figure 11: Feature absorption scores comparison of KronSAE vs baseline methods (TopK SAE and Matryoshka SAE) and a Kron-enhanced Matryoshka SAE variant.

Model	70M (d=512)		160M (d=768)		410M (d=1024)	
	Dictionary	65k	256k	65k	256k	65k
$m = 1$	0.893	0.892	0.856	0.855	0.834	0.835
$m = 2$	0.896	0.897	0.859	0.859	0.832	0.841
$m = 4$	0.894	0.899	0.857	0.859	0.828	0.839
$m = 8$	0.896	0.899	0.856	0.862	0.827	0.846
TopK	0.905	0.903	0.870	0.867	0.843	0.847

Table 4: Performance of SAEs on 70M, 160M and 410M Pythias with varying hidden dimensionality.

A.6 COMPARISON WITH JUMPRELU

We provide experiments to compare KronSAE with an alternative activation mechanism, JumpReLU, and report explained variance under three sparsity levels in Table 6.

Replacement of TopK with JumpReLU within KronSAE leads to a degraded performance relative to both JumpReLU SAE and KronSAE with TopK, also with degraded scaling over ℓ_0 . This suggests that the architectural advantages of KronSAE interact most effectively with TopK’s behaviour. Whether an alternative activation function can improve on this remains a topic for future work.

Model	SAE	$\ell_0 = 16$	$\ell_0 = 32$	$\ell_0 = 64$	$\ell_0 = 128$	$\ell_0 = 256$
Pythia	TopK	0.445	0.233	0.058	0.006	0.004
	KronSAE	0.244	0.129	0.033	0.007	0.003

Table 5: Absorption score calculated for Pythia 1.4B model. KronSAE shows lower score due to structured latent space and hierarchy between pre-latents and post-latents.

Model Variant	$\ell_0 = 32$	$\ell_0 = 50$	$\ell_0 = 64$
TopK	0.809	0.837	0.852
JumpReLU	0.813	0.838	0.844
KronSAE (TopK)	0.814	0.840	0.853
KronSAE (JumpReLU)	0.790	0.817	0.828

Table 6: Performance of SAEs with JumpReLU and TopK activations. Since we have floating sparsity controlled via ℓ_0 penalty coefficient, we performed a sweep over various sparsity levels, fitted a parabola to the resulting data as a function of ℓ_0 , and evaluated it on those sparsity levels. In contrast, TopK and KronSAE (with TopK) were trained using fixed, predefined sparsity levels.

A.7 PERFORMANCE ACROSS LAYERS

For this experiment we fix the dictionary size to $F = 2^{15}$ and use the same hyperparameters as in the main experiments. As the Figure 12 shows, KronSAE is on-par with TopK at every depth, demonstrating that structured encoder’s reconstruction quality is robust to layer choice.

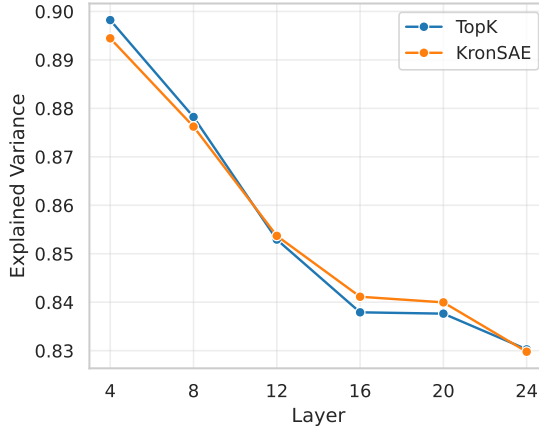


Figure 12: EV across layers of Qwen-2.5-1.5B, demonstrating that KronSAE matches TopK performance regardless of depth.

A.8 CHOICE OF m, n, h

We derive the following guidelines to train KronSAE: one should minimize the m and maximize the h to improve the reconstruction performance, and search for the most expressive configuration from feasible ones. Since m has more impact on EV, one should start from $m = 2$ in the search process, since it gives improved computational performance with on-par EV with full TopK training.

B MORE RESULTS ON SYNTHETIC

In this section we present the motivation behind our matching algorithm and additional results.

1026
1027

B.1 FEATURE MATCHING AS QUADRATIC PROBLEM

1028
1029
1030
1031

Suppose that we have two sets of feature embeddings from different models represented as matrices $X, Y \in \mathbb{R}^{F \times d}$, where F is the number of features and d is the dimensionality of feature embeddings. Our task is to find the optimal assignment between features from Y to features from X so that this assignment would satisfy some considerations.

1032
1033
1034
1035

The standard approach is to solve linear assignment problem - find a permutation matrix Π subject to minimizing the trace($C^T \Pi$), where C is a cost matrix defined as pairwise distance between features $C_{i,j} = d(X_i, Y_j)$. Standard algorithm for solving it in context of sparse dictionary learning is a Hungarian algorithm (Paulo & Belrose, 2025; Balagansky et al., 2025; Fel et al., 2025).

1036
1037
1038
1039
1040
1041

This linear problem is that it only considers pairwise information between features while ignoring the global dependencies between features within X and Y sets separately, e.g. clusters should map to clusters, and the linear problem does not internalize this information. Our observation of correlations between features naturally requires to search for assignment that would take this information into account: we seek for a permutation Π that would give best *global* alignment, measured as the Frobenius norm of $X^T \Pi Y$. So the objective becomes:

1042
1043
1044
1045

$$\max_{\Pi} \|X^T \Pi Y\|_F^2 = \max_{\Pi} \text{trace}(\Pi^T X X^T \Pi Y Y^T), \quad (8)$$

where global feature structure is explicitly encoded in the matrices XX^T and YY^T .

1046
1047
1048
1049
1050
1051

An efficient algorithm to solve the quadratic assignment problem is Fast Approximate Quadratic Programming (FAQ) method (Vogelstein et al., 2015) that initially was designed for graphs matching: given the adjacency matrices A and B , it minimizes the trace($A \Pi B^T \Pi^T$), where Π are relaxed from permutation matrices to the set of doubly stochastic matrices (Birkhoff polytope). In our case we define $A = XX^T$ and $B = YY^T$, and since we do not want to minimize the cost but rather maximize the similarity, we solve for the reversed objective:

1052
1053

$$\max_{\Pi} (XX^T \Pi (YY^T)^T \Pi^T) = \max_{\Pi} \text{trace}(\Pi^T X X^T \Pi Y Y^T), \quad (9)$$

1054
1055
1056

which is the same as equation 8, and this formulation preserves global dependencies because the contribution of assigning Y_j to X_i depends on all other assignments through the cross-terms in the quadratic form. Listing 1 shows the implementation of this matching procedure.

1057
1058

Listing 1: Implementation of FAQ algorithm for quadratic feature assignment problem.

```

1059 1 def feature_matching(A, B, max_iter):
1060 2     F, d = A.shape[0]
1061 3     G_A, G_B = A @ A.T, B @ B.T
1062 4     P = np.ones((F, F)) / F # Barycenter initialization
1063 5
1064 6     # Frank-Wolfe iterations
1065 7     for _ in range(max_iter):
1066 8         grad = 2 * G_A @ P @ G_B # Gradient for maximization
1067 9         r, c = linear_sum_assignment(-grad) # Solve LAP
106810         Q = np.zeros_like(P)
106911         Q[r, c] = 1
107012
107113         # Compute optimal step size
107214         D = Q - P
107315         b, a = np.trace(grad.T @ D), np.trace(G_A @ D @ G_B @ D.T)
107416
107517         if abs(a) < 1e-12:
107618             alpha = 1.0 if b > 0 else 0.0
107719         elif a < 0: # Concave case
107820             alpha = np.clip(-b/(2*a), 0, 1)
107921         else: # Convex case
22             alpha = 1.0 if b > 0 else 0.0
23
24         P_new = P + alpha * D
25         P = P_new
26

```

```

1080 27      # Project to permutation matrix
1081 28      r, c = linear_sum_assignment(-P)
1082 29      P_final = np.zeros((F, F))
1083 30      P_final[r, c] = 1
1084 31
1085 32      return P_final, P_final @ B

```

B.2 ADDITIONAL RESULTS

As shown in Figure 13, KronSAE maintains correlation structure that is heavier than in TopK and is better aligned with ground truth covariance matrix.

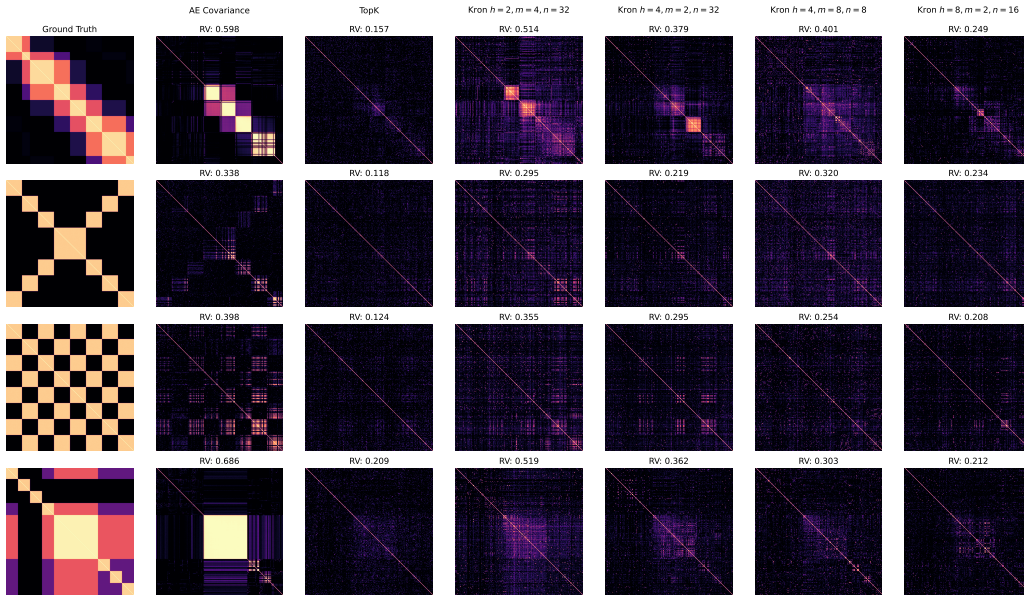


Figure 13: Examples of patterns learned in autoencoder TopK and KronSAE variants after we apply the improved matching scheme. KronSAE have learned patterns that more closely resemble the underlying ground truth structure, and with increasing number of heads (more fine-grained structure) it approaches the TopK SAE.

Table 7 indicate that structure learned by KronSAE is more diverse as indicated by standard deviation of the corresponding values, and is also more aligned with the ground truth covariance according to higher RV scores and lower differences (Δ) between properties of ground truth and learned matrix.

Model	RV coeff.	Effective rank	Mean corr.	Rank Δ
AE	0.59 ± 0.17	63.3 ± 0.3	0.13 ± 0.04	47.9
TopK	0.12 ± 0.02	58.5 ± 1.2	0.08 ± 0.01	43.2
Kron $h = 2, m = 4, n = 32$	0.22 ± 0.07	53.8 ± 3.4	0.08 ± 0.01	38.5
Kron $h = 4, m = 2, n = 32$	0.3 ± 0.12	46.0 ± 7.8	0.10 ± 0.03	30.7
Kron $h = 4, m = 8, n = 8$	0.23 ± 0.08	48.8 ± 5.0	0.09 ± 0.02	33.5
Kron $h = 8, m = 2, n = 16$	0.17 ± 0.04	55.9 ± 1.7	0.07 ± 0.01	40.6

Table 7: Results with improved matching scheme, computed for 8 different covariance setups. Higher RV coefficients between ground truth and learned matrices and lower Δ between properties of these matrices indicate that KronSAE is more variable across different setups and is better aligned with ground truth correlation structures.

Together, these results additionally validate improved covariance reconstruction in KronSAE.

1134 C mAND AS A LOGICAL OPERATOR AND KRONSAE AS LOGICAL SAE
11351136 **AND-like mechanism and hierarchy.** Suppose we have $\mathbf{u}^k = P^k \mathbf{x}$ and $\mathbf{v}^k = Q^k \mathbf{x}$. KronSAE can
1137 be described in two equivalent ways:1138 1. Applying the ReLU to latents \mathbf{u}, \mathbf{v} , then applying the Kronecker product and square root.
1139 2. Applying the mAND kernel that creates the matrix as in equation 3 and flattening it.
11401141 These approaches are complementary. To formally understand how they induce the AND-like
1142 mechanism and hierarchy, consider base and extension pre-latent vectors $\mathbf{p} = \text{ReLU}(\mathbf{u})$ and $\mathbf{q} =$
1143 $\text{ReLU}(\mathbf{v})$. Each p_i is a i th base pre-latent activation, and q_j is j th extension pre-latent activation.
1144 Kronecker product $\mathbf{p} \otimes \mathbf{q}$ creates the vector $(p_1 * q_1, \dots, p_1 * q_m, p_2 * q_1, \dots, p_n * q_m)$ of the
1145 activations of post-latents. Then there are two situations:
11461147 1. Post-latent is active \implies both pre-latents activations are positive.
1148 2. Post-latent is inactive \implies at least one of pre-latent activations is zero.
11491150 Hence post-latent is active only when both pre-latents are active. Fix some post-latent and its
1151 corresponding pre-latents, and suppose that $\mathcal{P}, \mathcal{Q}, \mathcal{F}$ are the sets of input vectors from the hidden
1152 state space (passed to SAE) on which base pre-latent, extension pre-latent and post-latent are active.
1153 Then it is true that $\mathcal{F} = \mathcal{P} \cap \mathcal{Q}$, meaning that pre-latents must be broader and polysemous to encode
1154 multiple semantics of emitted post-latents. We validate this behaviour qualitatively in section 5.3,
1155 although in the same section we describe that apparently other types of interactions also presented.
11561157 **Matryoshka and Kron hierarchy.** In contrast to TopK SAE, Matryoshka loss imposes different kind
1158 of hierarchy by dividing the dictionary into groups of G_1, \dots, G_k latents where each is of different
1159 level of granularity. Namely, first G_1 latents are the most broad and abstract, next G_2 latents add more
1160 fine-grained semantics, lowering the level of abstraction, and so on. This type of structure imposed by
1161 specific loss function - increasing the level of granularity must decrease the reconstruction error, and
1162 the lowest level of G_1 features must also maintain good reconstruction quality - and does not strictly
1163 demand some kind of conditional activation of features, while KronSAE imposes two-level AND-like
1164 hierarchy via architectural design (Kronecker product). As we have two different mechanisms of
1165 feature hierarchy (from encoding mechanism and loss function design) we can combine it, as shown
1166 in Section 4.1, 4.2 and Appendix A.4, to combine properties of both approaches.
11671168 **Visual intuition.** We also compare our mAND to existing AND_{AIL} (Lowe et al., 2021). Since our
1169 objective is to drive each atom toward a distinct, monosemantic feature, we found that tightening
1170 the logical conjunction encourages sharper feature separation. Moreover, by using the geometric
1171 mean (\sqrt{pq}) rather than a simple product or minimum, mAND preserves activation magnitudes and
1172 prevents post-latent activation to be exploded when both p, q are positive. A visual comparison of
1173 mAND and AND_{AIL} appears in Figure 14.1174 D FEATURE ANALYSIS METHODOLOGY
11751176 We analyze learned features using an established pipeline Bills et al. (2023); Paulo et al. (2024) con-
1177 sisting of three stages: (1) statistical property collection, (2) automatic activation pattern interpretation,
1178 and (3) interpretation evaluation. The following subsections detail our implementation.
11791180 D.1 DATA COLLECTION
11811182 Our collection process uses a fixed-size buffer $B = 384$ per feature, continuing until processing a
1183 predetermined maximum token count T_{max} . The procedure operates as follows:1184 Initial processing batches generate large activation packs of 1M examples, where each example
1185 comprises 256-token text segments. When encountering feature activations, we add them to the
1186 buffer, applying random downsampling to maintain size B when exceeding capacity. This approach
1187 enables processing arbitrary token volumes while handling rare features that may require extensive
1188 sampling.

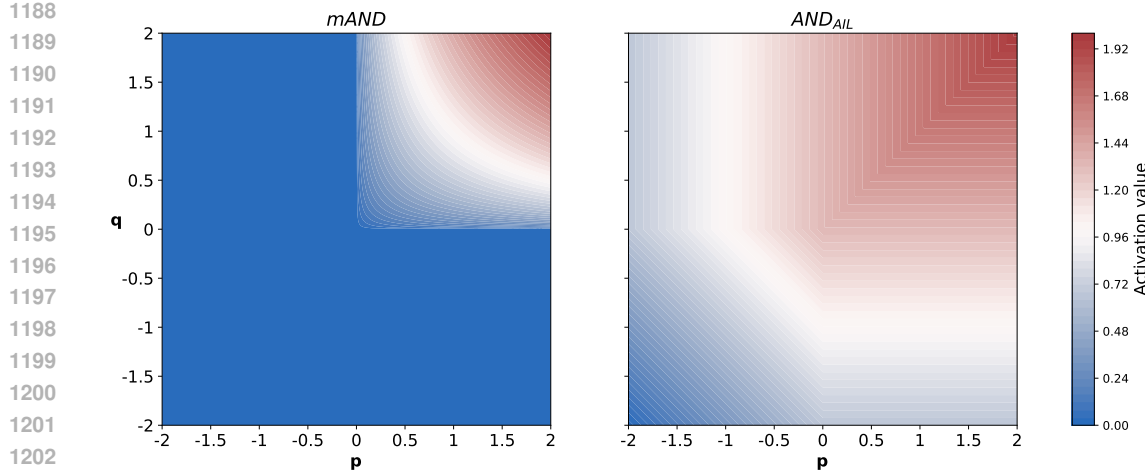


Figure 14: Comparison of the smooth mAND operator against the AND_{AIL} (Lowe et al., 2021).

During collection, we compute online statistics including activation minimums, maximums, means, and frequencies. Post-processing yields two key metrics: token entropy and multitoken ratio. The token entropy is calculated as:

$$\text{token entropy} = - \sum_{i=0}^n p_i \cdot \log(p_i), \quad p_i = \frac{\text{activations of token } i}{\text{total amount of activations}}, \quad (10)$$

where n represents unique activated tokens. The multitoken ratio is:

$$\text{multitoken ratio} = \frac{1}{b} \sum_{i=0}^b \frac{\text{number of activations in sequence } i}{\text{total tokens in sequence } i}, \quad (11)$$

with $b < B$ denoting collected context examples per feature.

We then segment examples using a 31-token context window (15 tokens before/after each activation), potentially creating overlapping but non-duplicated examples. Features with high multitoken ratio may have number of examples significantly exceeding B .

A separate negative examples buffer captures non-activating contexts. Future enhancements could employ predictive modeling (e.g., using frequent active tokens) to strategically populate this buffer with expected-but-inactive contexts, potentially improving interpretation quality.

D.2 FEATURE INTERPRETATIONS

For each feature, we generate interpretations by sampling 16 random activation examples above the median activation quantile and presenting them to Qwen3 14B (Yang et al., 2025) (AWQ-quantized with reasoning enabled). The model produces concise descriptions of the activation patterns. Empirical observations suggest reasoning mode improves interpretation quality, though we lack quantitative measurements. This aligns with findings in (Paulo et al., 2024), which compared standard one-sentence responses with Chain-of-Thought outputs, making model reasoning an interesting direction for future research.

The interpretation process uses the system prompt presented in Figure 15. User prompts include all special characters verbatim, as some features activate specifically on these characters. A representative (slightly abbreviated) user prompt example is presented on Figure 16.

1242
 1243
 1244 You are a meticulous AI researcher conducting an important
 1245 investigation into patterns found in language. Your task is
 1246 to analyze text and provide an explanation that thoroughly
 1247 encapsulates possible patterns found in it.
 1248
 Guidelines:
 1249
 1250 You will be given a list of text examples on which special
 1251 words are selected and between delimiters like «this». If a
 1252 sequence of consecutive tokens all are important, the entire
 1253 sequence of tokens will be contained between delimiters «just
 1254 like this». How important each token is for the behavior is
 1255 listed after each example in parentheses.
 1256
 - Your explanation should be a concise STANDALONE PHRASE that
 1257 describes observed patterns.
 1258 - Focus on the essence of what patterns, concepts and
 1259 contexts are present in the examples.
 1260 - Do NOT mention the texts, examples, activations or the
 1261 feature itself in your explanation.
 1262 - Do NOT write "these texts", "feature detects", "the
 1263 patterns suggest", "activates" or something like that.
 1264 - Do not write what the feature does, e.g. instead of
 1265 "detects heart diseases in medical reports" write "heart
 1266 diseases in medical reports".
 1267 - Write explanation in the last line exactly after the
 1268 [EXPLANATION]:
 1269
 1270 Figure 15: System prompt for feature interpretations.
 1271
 1272
 1273

1274 Examples of activations:
 1275
 1276 Text: ' Leno«,» a San Francisco Democrat«, said in a
 1277 statement.»'
 1278 Activations: ' said (22.74), statement (27.84), in (27.54)'
 1279
 1280 Text: ' city spokesman Tyler Gamble« said in an» email.'
 1281 Activations: ' said (2.92), in (12.81), an (14.91)'
 1282
 1283 Text: ' towpath at Brentford Lock. «Speaking» on BBC
 1284 London 94'
 1285 Activations: 'Speaking (3.48)'
 1286
 1287 Text: ' Michelle, a quadriplegic,« told» DrBicuspid.com'
 1288 Activations: ' told (4.05)'
 1289
 1290 Text: ' CEO Yves Carcelle« said in a statement.»'
 1291 Activations: ' said (19.64), in (29.09), statement (29.39)'
 1292
 1293
 1294
 1295

Figure 16: Example of user prompt passed to LLM. This feature with 16 examples received the interpretation "*Structural elements in discourse, including speech attribution, prepositional phrases, and formal contextual markers*" with a detection score of 0.84 and fuzzing score of 0.76.

1296
1297

D.3 EVALUATION PIPELINE

1298
1299
1300
1301
1302
1303

We evaluate interpretations using balanced sets of up to 64 positive (activation quantile > 0.5) and 64 negative examples, employing the same model without reasoning to reduce computational costs. When insufficient examples exist, we maintain class balance by equalizing positive and negative counts. The evaluation uses modified system prompts from (Paulo et al., 2024), with added emphasis on returning Python lists matching the input example count exactly. We discard entire batches if responses are unparseable or contain fewer labels than the number of provided examples.

1304
1305
1306
1307
1308

We calculate two scores.

1309
1310

Detection Score: After shuffling positive/negative examples, we present up to 8 unformatted text examples per batch to the model. The model predicts activations (1/0) for each example, generating up to 128 true/predicted label pairs. The score calculates as:

$$\text{score} = \frac{1}{2} \left(\frac{\text{correctly predicted positives}}{\text{total positives}} + \frac{\text{correctly predicted negatives}}{\text{total negatives}} \right). \quad (12)$$

1311
1312
1313
1314
1315

Fuzzing Score: We «highlight» activated tokens on sampled examples, from which 50% are correctly labeled positive examples, 25% are mislabeled positive examples, and 25% are randomly labeled negative examples. We present batches of up to 8 examples and the model identifies correct/incorrect labeling, with scoring following Equation 12.

1316
1317

E ADDITIONAL FEATURE ANALYSIS RESULTS

1318
1319
1320
1321
1322
1323
1324

Feature property correlations. Our analysis reveals significant correlations between feature properties and interpretability scores (Figure 17). Notably, token entropy and mean activation show substantial correlations with interpretability scores, suggesting their potential as proxies for assessing feature quality without running the full interpretation pipeline. These findings are based on analysis of the first 3072 features from 32k TopK and KronSAE ($m=4, n=4$) trained on 24M tokens, warranting further validation with larger-scale studies.

1325
1326
1327
1328
1329

Pre-latent to post-latent relationships. We investigate how post-latent properties correlate with various combinations of pre-latent properties, including individual values, means, products, and the mAND operation (product followed by square root). Figure 18 demonstrates that post-latent multitoken ratio, token entropy, and frequency show stronger correlations with pre-latent products or mAND values than with individual pre-latent properties or their means.

1330
1331
1332
1333
1334
1335
1336

Basis geometry. As noted in Section 5.3, latent embeddings primarily exhibit clustering within their originating groups (head, base, extension). With the support of observations reported in Sections 4.1 and 5.3, we find that models with more heads achieve better reconstruction while producing more diverse basis vectors. This suggests that fine-grained architectures yield more expressive representations, although they may also exhibit undesired challenging behavior like feature splitting (Bricken et al., 2023) or absorption (Chanin et al., 2024).

1337
1338
1339
1340

Figure 19 visualizes this structure through UMAP projections ($n_{\text{neighbors}}=15, \text{min_dist}=0.05$, metric='cosine') of decoder weights from the first 8 heads of 32k SAEs with varying m, n configurations. The plots reveal distinct clustering patterns: for $m < n$ we observe tight base-wise clustering with weaker grouping by extension, and for $m \geq n$ extension-wise clustering is stronger.

1341
1342
1343
1344

This asymmetry suggests that pre-latent capacity requirements directly manifest in the embedding geometry - components with lower polysemy (extensions when $m < n$) exhibit greater geometric diversity. We expect symmetric behavior for reciprocal configurations (e.g., $m=4, n=8$ vs. $m=8, n=4$), merely swapping the roles of bases and extensions.

1345
1346
1347
1348
1349

Interpretability across sparsity regimes. We compare KronSAE and its Matryoshka variant with TopK, Matryoshka and Switch SAE baselines across different sparsity regimes for Gemma 2 2B and Qwen 2.5 1.5B. For each SAE we follow the same pipeline as for results in Section 5.3, but use only 18 million tokens for examples collection. For KronSAE and TopK we use first 4096 features, and

	TopK - Pearson							KronSAE Post - Pearson							KronSAE Pre - Pearson						
	Mean score	0.93	0.87	0.50	-0.41	-0.18	-0.24	1.00	0.94	0.88	0.54	-0.39	-0.08	-0.20	1.00	0.93	0.88	0.55	-0.44	-0.39	-0.29
Detection score	0.93	1.00	0.63	0.45	-0.34	-0.14	-0.25	0.94	1.00	0.66	0.49	-0.33	-0.05	-0.20	0.93	1.00	0.65	0.49	-0.34	-0.34	-0.26
Fuzzing score	0.87	0.63	1.00	0.48	-0.43	-0.20	-0.17	0.88	0.66	1.00	0.49	-0.43	-0.13	-0.16	0.88	0.65	1.00	0.53	-0.47	-0.37	-0.22
Mean activation	0.50	0.45	0.48	1.00	-0.32	-0.15	-0.09	0.54	0.49	0.49	1.00	-0.34	-0.01	-0.08	0.55	0.49	0.53	1.00	-0.43	-0.39	-0.17
Token entropy	-0.41	-0.34	-0.43	-0.32	1.00	0.35	0.23	-0.39	-0.33	-0.43	-0.34	1.00	0.42	0.21	-0.44	-0.34	-0.47	-0.43	1.00	0.49	0.29
Multitoken ratio	-0.18	-0.14	-0.20	-0.15	0.35	1.00	0.51	-0.08	-0.05	-0.13	-0.01	0.42	1.00	0.35	-0.39	-0.34	-0.37	-0.39	0.49	1.00	0.51
Frequency	-0.24	-0.25	-0.17	-0.09	0.23	0.51	1.00	-0.20	-0.20	-0.16	-0.08	0.21	0.35	1.00	-0.29	-0.26	-0.22	-0.17	0.29	0.51	1.00
	TopK - Spearman							KronSAE Post - Spearman							KronSAE Pre - Spearman						
	Mean score	0.93	0.87	0.61	-0.45	-0.15	-0.27	1.00	0.93	0.88	0.68	-0.43	-0.03	-0.23	1.00	0.93	0.88	0.59	-0.45	-0.38	-0.47
Detection score	0.93	1.00	0.64	0.56	-0.38	-0.10	-0.31	0.93	1.00	0.66	0.62	-0.37	0.03	-0.26	0.93	1.00	0.65	0.53	-0.37	-0.33	-0.45
Fuzzing score	0.87	0.64	1.00	0.56	-0.46	-0.19	-0.16	0.88	0.66	1.00	0.60	-0.47	-0.10	-0.14	0.88	0.65	1.00	0.56	-0.47	-0.39	-0.41
Mean activation	0.61	0.56	0.56	1.00	-0.37	-0.27	-0.31	0.68	0.62	0.60	1.00	-0.40	-0.03	-0.25	0.59	0.53	0.56	1.00	-0.53	-0.57	-0.64
Token entropy	-0.45	-0.38	-0.46	-0.37	1.00	0.35	0.31	-0.43	-0.37	-0.47	-0.40	1.00	0.38	0.36	-0.45	-0.37	-0.47	-0.53	1.00	0.52	0.46
Multitoken ratio	-0.15	-0.10	-0.19	-0.27	0.35	1.00	0.73	-0.03	0.03	-0.10	-0.03	0.38	1.00	0.63	-0.38	-0.33	-0.39	-0.57	0.52	1.00	0.85
Frequency	-0.27	-0.31	-0.16	-0.31	0.31	0.73	1.00	-0.23	-0.26	-0.14	-0.25	0.36	0.63	1.00	-0.47	-0.45	-0.41	-0.64	0.46	0.85	1.00
	Mean score	Detection score	Fuzzing score	Mean activation	Token entropy	Multitoken ratio	Frequency	Mean score	Detection score	Fuzzing score	Mean activation	Token entropy	Multitoken ratio	Frequency	Mean score	Detection score	Fuzzing score	Mean activation	Token entropy	Multitoken ratio	Frequency

Figure 17: Correlation coefficients (Pearson and Spearman) between properties of TopK and KronSAE latents. Token entropy emerges as a strong predictor of interpretability scores, while higher mean activation and lower frequency also indicate more interpretable features.

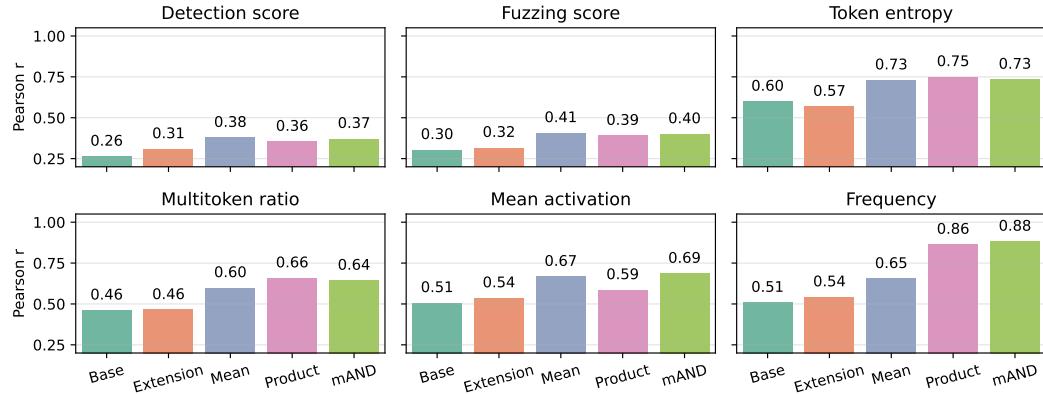


Figure 18: Correlation patterns between properties of post-latents and pre-latents.

for other models we sample 4096 features randomly. Scores for $F = 2^{16}$ and $F = 2^{15}$ are presented in Figures 20 and 21.

Results show that TopK and KronSAE are very stable across both models and sparsity regimes, while for other models their architectural and training design significantly affect the interpretability.

We attribute those differences between Gemma and Qwen to different capacity of residual stream - Gemma has hidden state size of 2304, while Qwen has only 1536 dimensions (1.5x smaller). However, differences between training data and architectural choices can also be the cause.

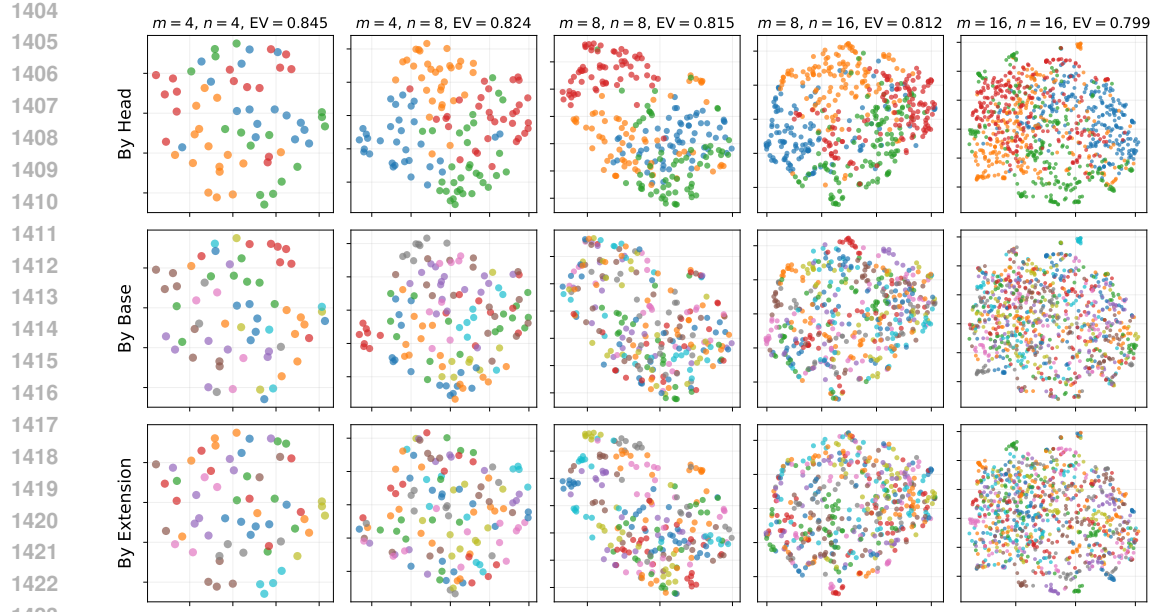


Figure 19: UMAP visualization of post-latent clustering patterns by head, base, and extension group membership. We observe tight clusters by base for $m < n$ and by extension for $m \geq n$.

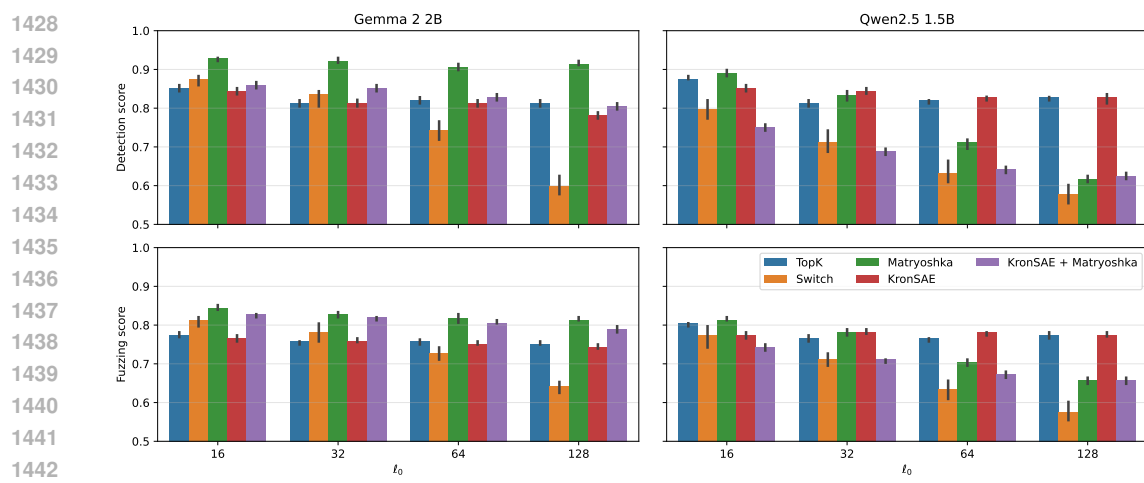


Figure 20: Interpretability scores for $F = 2^{16} = 65536$. KronSAE shows good consistency across different sparsity regimes, in some cases outperforming the TopK baseline.

Interpretability tradeoff. As shown in Section 4.1 KronSAE introduces tradeoff between computational efficiency, explained variance and interpretability. We can force more features to be correlated in same head by increasing the m and n , and this will improve computational efficiency, but at the cost of reconstruction performance; however, improving the explained variance (with small m and fine-grained structure of groups) goes with the cost of slight reduction in the interpretability. These tradeoffs are expected and presented across variety of SAEs (Karvonen et al., 2025).

To evaluate how KronSAE behave under different m, n we compute autointerpretability scores following the same setup as described in Appendix D for Qwen-2.5 1.5B and Gemma-2 2B models with sparsity $\ell_0 \in \{16, 32, 64, 128\}$. As Figure 22 shows, setup $m = 1$ and $h = 4096$ is less interpretable than $m = 2$ and $m = 4$ with the same number of heads despite having stronger reconstruction performance.

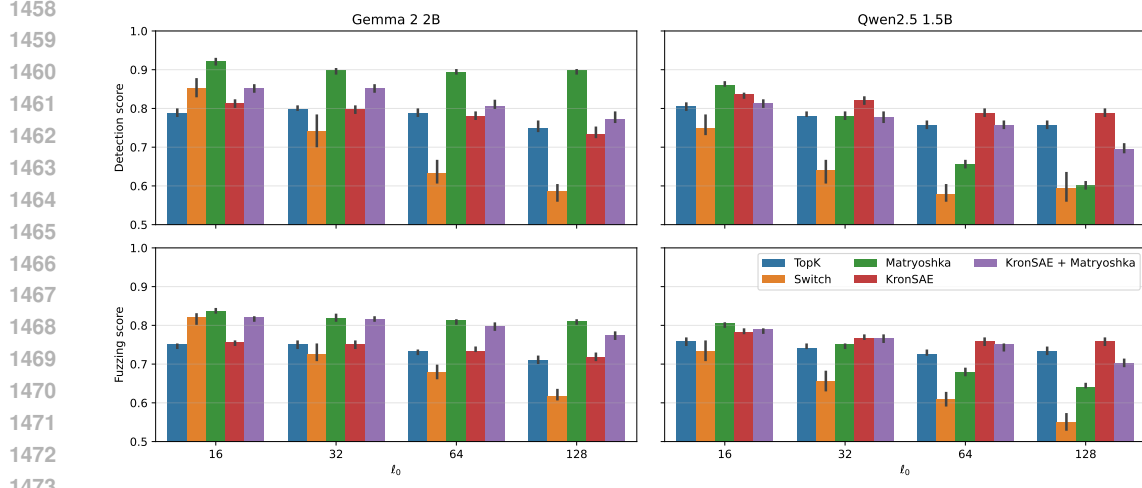


Figure 21: Interpretability scores for $F = 2^{15} = 32768$. KronSAE shows good consistency across different sparsity regimes, in some cases outperforming the TopK baseline. The result is the same as for 65k dictionary size at the Figure 20, but with slightly lower scores.

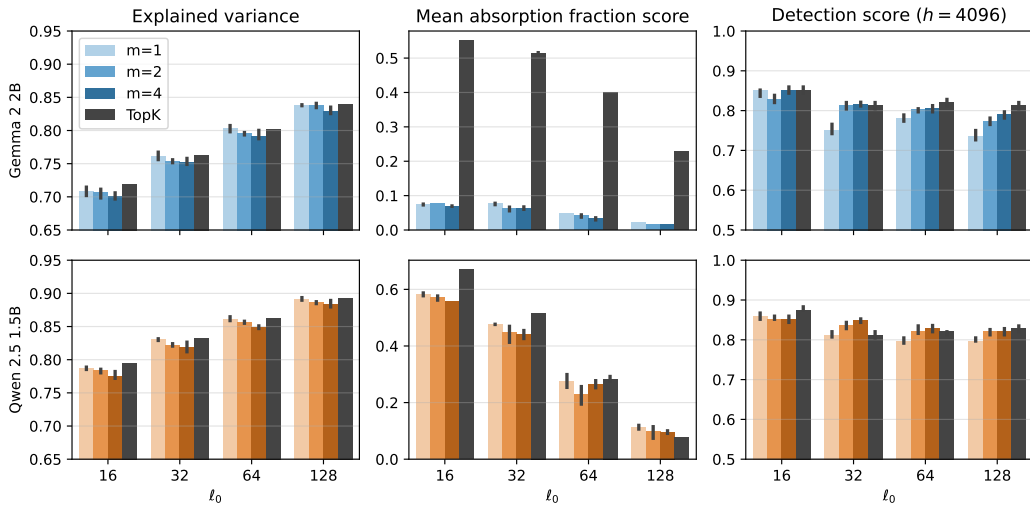


Figure 22: EV, absorption score and interpretability for $F = 2^{16}$. For constant h , decreasing m leads to lower interpretability scores and absorption scores, but increase EV - this is expected due to increasing polysemy of pre-latents and entanglement of the features. See Section 5.3 for a explanation of the retrieval mechanism.

F KRONSAE IN TERMS OF TENSOR DIAGRAM

The proposed encoder architecture can be visualized as a tensor diagram (Figure 23). Notably, this formulation draws a connection to quantum mechanics, where $|\mathbf{f}\rangle$ represents the (unnormalized) state of two disentangled qubits described by $|\mathbf{p}\rangle$ and $|\mathbf{q}\rangle$.

If we were to sum the outputs of the encoder's heads instead of concatenating them, $|\mathbf{f}\rangle$ would correspond to a separable quantum state. This scenario can be expressed via the Schmidt decomposition:

$$|\mathbf{f}\rangle = \sum_h |\mathbf{p}_h\rangle \otimes_K |\mathbf{q}_h\rangle,$$

where \otimes_K denotes the Kronecker product. However, preliminary experiments revealed that this alternative design results in poorer performance compared to the concatenation-based approach.

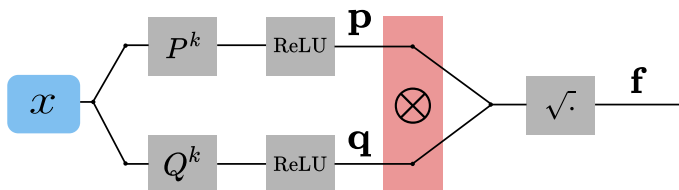


Figure 23: For a single head, the KronSAE encoder architecture separates the input x into two distinct components, p and q , via matrix multiplications P^k and Q^k accordingly, followed by ReLU activation. These components are then combined via the Kronecker product $p \otimes q$ and square root operation $\sqrt{\cdot}$, resulting in an output vector f .

G ANALYSIS OF COMPOSITIONAL STRUCTURE

Here we analyze more examples of interactions in various heads.

Head 3. For this head we have selected all base elements and extension 2, shown in Table 8. Extension element 2 shows moderate interpretability with clear AND-like interactions: with base 1 (semantic inheritance through shared pre-latent semantics) and base 2 (retaining only instrument-related semantics). Notable interactions occur with base 0 (acquiring medical semantics while preserving metric/number aspects) and base 3 (combining instrument semantics with necessity to yield therapy/treatment concepts). The high interpretability scores suggest potential additional encoding mechanisms beyond simple intersection, possibly related to activation magnitude, though dataset or interpretation artifacts cannot be ruled out without further validation.

Component	Interpretation	Score
Extension 2	Scientific instruments, acronyms, and critical numerical values in technical and astronomical contexts	0.71
Base elements and their compositions with extension 2		
Base 0	<i>Interpretation:</i> Punctuation marks and line breaks serving as structural separators in text. <i>Composition:</i> Health-related metrics focusing on survival rates, life expectancy, and longevity.	0.66
Base 1	<i>Interpretation:</i> Numerical values, both in digit form and as spelled-out numbers, often accompanied by punctuation like decimals or commas, in contexts of measurements, statistics, or quantitative expressions. <i>Composition:</i> Numerical digits and decimal points within quantitative values.	0.80
Base 2	<i>Interpretation:</i> Nuanced actions and adverbial emphasis in descriptive contexts. <i>Composition:</i> Astronomical instruments and their components, such as space telescopes and their acronyms, in scientific and observational contexts.	0.71
Base 3	<i>Interpretation:</i> Forms of the verb "to have" indicating possession, necessity, or occurrence in diverse contexts. <i>Composition:</i> Antiretroviral therapy components, viral infection terms, and medical treatment terminology.	0.91

Table 8: Interactions between extension 2 in head 3 and all base elements in that head.

1566
 1567
 1568
Head 136. This head exhibits higher interpretability in post-latents than pre-latents. Key observa-
 1569
 tions from the Table 9 include: extension 2 with base 0 narrows semantics to Illinois (likely inheriting
 1570
 geographical subsemantics), while interactions with bases 2-3 demonstrate complexity beyond simple
 1571
 intersection, often introducing additional semantics requiring deeper investigation.

Component	Interpretation	Score
Extension 2	Hierarchical scopes, geographic references, and spatial dispersal terms	0.78
Base elements and their compositions with extension 2		
Base 0	<i>Interpretation:</i> Numerical decimal digits in quantitative expressions and proper nouns. <i>Composition:</i> The state of Illinois in diverse contexts with high significance.	0.79
Base 1	<i>Interpretation:</i> The number three and its various representations, including digits, Roman numerals, and related linguistic forms. <i>Composition:</i> Geographic place names and their linguistic variations in textual contexts.	0.84
Base 2	<i>Interpretation:</i> Ordinal suffixes and temporal markers in historical or chronological contexts. <i>Composition:</i> Terms indicating layers, degrees, or contexts of existence or operation across scientific, organizational, and conceptual domains.	0.87
Base 3	<i>Interpretation:</i> Question formats and topic introductions with specific terms like "What", "is", "of", "the", "Types", "About" in structured text segments. <i>Composition:</i> Spatial spread and occurrence of species or phenomena across environments.	0.77

Table 9: Interactions between extension 2 in head 136 and all base elements in that head.

1593
 1594
 1595
Head 177. Latents presented in Table 10 emonstrates more consistent AND-like behavior than
 1596
 Heads 3 and 136, closely matching the interaction pattern shown in Figure 2.

Component	Interpretation	Score
Extension 1	Geographical mapping terminology and institutional names, phrases involving spatial representation and academic/organizational contexts	0.90
Base elements and their compositions with extension 1		
Base 0	<i>Interpretation:</i> Proper nouns, abbreviations, and specific named entities. <i>Composition:</i> Geographical or spatial references using the term "map".	0.64
Base 1	<i>Interpretation:</i> Emphasis on terms indicating feasibility and organizations. <i>Composition:</i> Specific organizations and societal contexts.	0.80
Base 2	<i>Interpretation:</i> Institutional names and academic organizations, particularly those containing "Institute" or its abbreviations, often paired with prepositions like "of" or "for" to denote specialization or affiliation. <i>Composition:</i> Institutional names containing "Institute" as a core term, often followed by prepositions or additional descriptors.	0.89
Base 3	<i>Interpretation:</i> Closure and termination processes, initiating actions. <i>Composition:</i> Initiating or establishing a state, direction, or foundation through action.	0.79

Table 10: Interactions between extension 1 in head 177 and all base elements in that head.

1620 H KRONSAE SIMPLIFIED IMPLEMENTATION

```

1621
1622
1623 1 class KronSAE(nn.Module):
1624 2     def __init__(self, config):
1625 3         super().__init__()
1626 4         self.config = config
1627 5         _t = torch.nn.init.normal_
1628 6             torch.empty(
1629 7                 self.config.act_size,
1630 8                 self.config.h * (self.config.m + self.config.n)
1631 9             )
1632 10        ) / math.sqrt(self.config.dict_size * 2.0)
1633 11        self.W_enc = nn.Parameter(_t)
1634 12        self.b_enc = nn.Parameter(
1635 13            torch.zeros(self.config.h * (self.config.m + self.config.n))
1636 14        )
1637 15        W_dec_v0 = einops.rearrange( # Initialize decoder weights
1638 16            _t.t().clone(), "(h mn) d -> h mn d",
1639 17            h=self.config.h, mn=self.config.m + self.config.n
1640 18        )[:, :self.config.m]
1641 19        W_dec_v1 = einops.rearrange(
1642 20            _t.t().clone(), "(h mn) d -> h mn d",
1643 21            h=self.config.h, mn=self.config.m + self.config.n
1644 22        )[:, self.config.m:]
1645 23        self.W_dec = nn.Parameter(einops.rearrange(
1646 24            W_dec_v0[..., None, :] + W_dec_v1[..., None, :, :],
1647 25            "h m n d -> (h m n) d"
1648 26        ))
1649 27        self.W_dec.data[:] =
1650 28            self.W_dec.data / self.W_dec.data.norm(dim=-1, keepdim=True)
1651 29        )
1652 30        self.b_dec = nn.Parameter(torch.zeros(self.config.act_size))
1653 31
1654 32        def encode(self, x: torch.Tensor) -> torch.Tensor:
1655 33            B, D = x.shape
1656 34            acts = F.relu(
1657 35                x @ self.W_enc + self.b_enc
1658 36            ).view(B, self.h, self.m + self.n)
1659 37            all_scores = torch.sqrt(
1660 38                acts[..., :self.config.m, None] * \
1661 39                    acts[..., self.config.m:, None, :] + 1e-5
1662 40            ).view(B, -1)
1663 41            scores, indices = all_scores.topk(
1664 42                self.config.k, dim=-1, sorted=False
1665 43            )
1666 44            acts_topk = torch.zeros(
1667 45                (B, self.config.dict_size)
1668 46            ).scatter(-1, indices, scores)
1669 47            return acts_topk
1670 48
1671 49        def forward(self, x):
1672 50            acts_topk = self.encode(x)
1673 51            x_rec = acts_topk @ self.W_dec + self.b_dec
1674 52            output = self.get_loss_dict(x, x_rec)
1675 53            return output
1676 54
1677 55        def get_loss_dict(self, x, x_rec):
1678 56            loss = (x_rec - x.pow(2).mean())
1679 57            pt_12 = (x_rec - x).pow(2).sum(-1).squeeze()
1680 58            var = (x - x.mean(0)).pow(2).sum(-1).squeeze()
1681 59            ev = (1 - pt_12 / var).mean()
1682 60            return loss, ev

```

1674 **I USAGE OF LARGE LANGUAGE MODELS**
16751676 We have used LLMs as the main tool for conducting the interpretability experiments, as described in
1677 section D, and as the instrument for language polishing and word choice.
1678

1679

1680

1681

1682

1683

1684

1685

1686

1687

1688

1689

1690

1691

1692

1693

1694

1695

1696

1697

1698

1699

1700

1701

1702

1703

1704

1705

1706

1707

1708

1709

1710

1711

1712

1713

1714

1715

1716

1717

1718

1719

1720

1721

1722

1723

1724

1725

1726

1727